Wavefront assessment and correction of the rat eye for two photon excitation therapies

by

Ian Andrews

A thesis
presented to the University of Waterloo
in fulfillment of the
thesis requirement for the degree of
Masters of Science
in
Physics

Waterloo, Ontario, Canada, 2016

This thesis consists of material all of which I authored or co-authored: see Statement of Contributions included in the thesis. This is a true copy of the thesis, including any required final revisions, as accepted by my examiners.

I understand that my thesis may be made electronically available to the public.

Statement of Contributions

I would like to acknowledge the names of my actual and potential co-authors who contributed to my research described in this thesis, these include:

- Marsha L. Kisilak
- Laura Emptage
- Kait Bunghardt
- Dr. Kevin Resch
- Dr. Melanie CW Campbell

The work presented in this thesis was based on the work done previously by Mark Bird in his 2006 thesis on "Modelling light delivery into the rat eye for two-photon excitation photodynamic therapy treatment of age-related macular degeneration," and Dr. Mamta Khurana in her 2010 thesis, "Two-Photon Excitation Photodynamic Therapy for Localized Blood Vessel Targeting." Dr. Campbell provided the background understanding of the rat eye, knowledge of ophthalmoscopic imaging and adaptive optics. Dr. Kevin Resch provided laboratory space and equipment necessary for experiments as well as guidance in usinig the equipment. Marsha L. Kisilak provided knowledge and skills required to acquire retinal images of an anesthetized rat as well as the operation of experimental equipment. Laura Emptage and Kait Bunghardt both contributed to animal handling and assisted in carrying out experimental procedures.

As the author of this thesis, I provided the design and construction of the experimental apparatus as well as conducted the experimental procedures to acquire retinal images and Hartmannn-Shack measurements of the rat eye. I also extended the schematic rat eye model in Zemax, with rigid contact lenses. I analysed the new schematic rat eye and compared the image quality improvement with the original schematic eye model. I wrote my findings in this thesis after discussion with Dr. Campbell about the interpretation of the data. Dr. Campbell also provided suggested revisions of the thesis and oversaw changes requested by my committee.

Abstract

Photodynamic therapy (PDT) is a treatment in which light excites a photosensitive drug to produce oxygen radicals that kills nearby cells. Today, PDT's is most commonly used application is for the destruction of cancerous tumor cells in humans, however it can also be used to treat the eye disease, age-related macular degeneration (AMD). One-photon excitation PDT treatment of AMD has not been found to successfully improve vision quality due to the revascularization in the retina which occurs post-treatment. Two-photon excitation (TPE) has been explored as an alternative because it may prevent revascularization of the retina post-treatment and provides more precise treatment localization. The rat eye has been selected as the optical model for testing TPE of a photosensitive drug, however the rat eye suffers from poor tear film quality and large optical aberrations requiring adaptive optics to improve retinal image quality and the probability of TPE. *In vivo* testing of the excitation of a photosensitive drug via TPE is an important step towards successful treatment of AMD in the human eye.

In this thesis, the design of an adaptive optics scanning laser ophthalmoscope for two photon light delivery is outlined, retinal images and wavefront error correction of the rat eye using a Xinetics 37-channel deformable mirror are presented. The extension of a schematic rat eye model to include a contact lens and tear lens predicts improved image quality at

the retina for a larger pupil size. During the course of this project, changes in refractive error and retinal image quality while using different contact lenses were observed. Based on the model and experimental observations, the use of rigid contact lenses was shown to improve retinal image quality of the rat eye and therefore the probability of TPE in the rat eye, prior to the use of adaptive optics.

Acknowledgements

This thesis would not be possible without the financial support of the following sources: University of Waterloo; and the National Sciences and Engineering Research Council of Canada.

I would first like to thank my supervisor, Dr. Melanie Campbell for her support throughout my undergraduate and graduate degree programs. She provided valuable guidance and encouragement, an immense knowledge base, and challenged me in my studies. To my committee members, my thanks to Dr. Donna Strickland for providing me with guidance throughout my undergraduate and graduate career. Dr. Kevin Resch for allowing me space in his laboratory and use of his equipment.

I would like to thank my colleagues in Campbell Labs at the University of Waterloo: Marsha Kisilak, for her assistance with the CSLO, all of the administrative tasks and for being a source of continual support. To Laura Emptage and Kait Bunghardt for their assistance with acquiring images in many experiments. To Nancy Gibson of the animal care facilities who taught me animal care ethics and procedures. To Mark Bird who assisted me with the optical software Zemax, and his prior work on this project.

To Alison Cheeseman and Shawn Dion for editing my thesis, and providing incredible support throughout this two year project. Your continual support has had a huge impact

on my research career.

Thanks to Spin Ice, UW semi-competitive hockey team champions of 2015, for providing me with a great team atmosphere, and to the University of Waterloo OSA student chapter for creating and constructing the successful Light Illuminated museum exhibit. Both groups have provided me with relief from the stress of studying and we have created some unforgettable memories together. Thank you.

Finally I would like to thank my parents, Paul and Elaine Andrews for allowing me the opportunity to study at a university level. To my brother, Simon who has been my mentor. Thank you.

Dedication

This thesis is dedicated to my parents, who provided unconditional support.

Table of Contents

List of Tables **xvii**

List of Figures **xix**

1 Introduction **1**

1.1 Age-Related Macular Degeneration 1

1.2 Photodynamic Therapy 2

1.3 Overview 6

2 Two Photon Excitation Delivery Apparatus **9**

2.1 Wavefront Measurement 10

2.2 Theory of Hartmann-Shack Wavefront Sensor 10

2.3 Dynamic Range and Sensitivity 13

2.4 Wavefront and Zernike Polynomials 14

2.5 Retinal imaging with adaptive optics 17

2.6 Wavefront corrector: Xinetics 37-actuator deformable mirror 19

2.7 Adaptive optics correction of the rat eye . . . 21
2.8 Apparatus design . . . 23
2.8.1 Confocal scanning laser ophthalmoscope (CSLO) . . . 23
2.8.2 Hartmann-Shack (HS) wavefront sensor . . . 25
2.8.3 Treatment beam . . . 26
2.9 Design Specifications, Constraints and Improvements . . . 28
2.9.1 Minimizing the system aberrations due to the integration of the Xinetics deformable mirror . . . 29
2.9.2 Verifying that the HS and treatment delivery optical paths are diffraction-limited . . . 31
2.10 Conclusions . . . 32

3 Imaging and wavefront sensing of the rat eye **35**

3.1 Methods . . . 36
3.2 Results . . . 37
3.2.1 Initial attempt at imaging and wavefront sensing of the rat eye . . . 37
3.2.2 Demonstration of wavefront correction of the rat eye . . . 38
3.2.3 Eye movement . . . 41
3.3 Discussion . . . 43
3.3.1 Noise in the Hartmann-Shack spot patterns . . . 43

3.3.2 Determining the sensing plane of the Hartmann-Shack wavefront sensor 44

3.3.3 Wavefront correction of the Long-Evans rats 45

3.4 Conclusions 47

4 The Effect of Rigid Contact Lens Parameters on Wavefront Aberration of the Rat Eye 49

4.1 Optical Model 52

4.2 Methods 54

4.2.1 Rats and preparation for in vivo imaging 54

4.2.2 Hartmann-Shack measurements of the rat eye and extending the Campbell model with a contact lens 55

4.3 Results 56

4.4 Hartmann-Shack measurements of the rat eye with contact and spectacle lens correction 56

4.4.1 Optical Modelling: Varying the base curvature of the contact lenses with constant paraxial power on the elliptical shell model of the rat eye 60

4.4.2 Further optical modelling of the rat eye 69

4.5 Discussion 71

4.5.1 Comparing Refractive Error Measurements to the Elliptical Shell Model 71

4.5.2 The Effects of Contact Lenses on the Optical Quality of the Rat eye 72

4.5.3 Utilizing the contact lens for improved image quality and two-photon excitation 74

4.6 Conclusions 75

5 Discussion and Conclusions **77**

5.1 Discussion 77

5.2 Conclusions 81

6 Permissions **83**

References **85**

List of Tables

2.1 Table of Zernike polynomials up to fourth order including names 17

4.1 Campbell and Hughes (1982) schematic rat eye model 54

4.2 A table of contact lens radii, nominal power and effective power due to spherical aberration for different 2mm and 3.5mm aperture 60

4.3 Effective power of the contact lens and tear lens combination 63

List of Figures

1.1 The Jablonski diagram for Photodynamic Therapy, image courtesy of Dr. M. Khurana with permission 3

1.2 One-photon vs. two-photon excitation diagram 4

2.1 Cross sectional view of a plane wavefront incident on a lenslet array 12

2.2 Cross sectional view of an aberrated wavefront incident on a lenslet array . 12

2.3 A layout of adaptive optics closed loop system for light delivery and improved imaging resolution 19

2.4 Image of the Xinetics 37-actuator deformable mirror 20

2.5 Ray diagram of the Confocal Scanning Laser Ophthalmoscope 24

2.6 Hartmann-Shack layout for a non-scanning wavefront-sensing beacon . . . 27

2.7 Astigmatism due to two off-axis spherical mirror telescopes 30

2.8 Diffraction limited point spread function of the Hartmann-Shack optical path from the rat eye to the CCD camera 32

3.1 Hartmann-Shack spot pattern of rat eye with noise 38

3.2 Second order wavefront correction with adaptive optics over 100 frames . . 39

3.3 Hartmann-Shack spot pattern of an adaptive optics corrected wavefront aberration 40

3.4 Higher order aberrations before and after adaptive optics corrections over 100 frames 41

3.5 Eye movement laterally shifted images caused by respiration moving the entire body and head of the rat 42

4.1 Schematic of the Campbell elliptical shell model. The figure was adapted from Bird. 53

4.2 Hartmann-Shack pattern of rat eye with 15.8D of correction with a spectacle lens 57

4.3 Hartmann-Shack pattern of rat eye with 12D contact lens and residual 6D defocus 58

4.4 Hartmann-Shack spot pattern of rat eye corrected with a +12D contact lens and -1D spectacle lens demonstrating very sharp spots. 59

4.5 Campbell and Hughes (1982) schematic rat eye model modified with a contact lens and associated tear lens 62

4.6 Flat contact lens base curvature relative to the corneal curvature 62

4.7 Steep contact lens base curvature relative to the corneal curvature 62

4.8 A plot of the spectacle lens power required to move focus to retinal surface for varying base curvatures of contact lenses for the Elliptical Shell model . 65

4.9 A plot of the strehl ratio versus the base curvature of the rigid contact lenses ranging from 10D to 20D for the elliptical shell rat eye model, 115 day old rat 66

4.10 A plot of the spherical aberration versus the base curvature of rigid contact lenses ranging from 10D to 20D for the elliptical shell model, 115 day old rat 67

4.11 A plot of the Strehl ratio vs. spherical aberration of the Elliptical Shell model for a range of contact lenses 69

Chapter 1

Introduction

1.1 Age-Related Macular Degeneration

Age-Related Macular Degeneration (AMD) is a disease that is the deterioration of the macula layer of the retina. The macula is at the center of the retina and contains the fovea, the densest area of photoreceptors. The clinical marker of AMD is the presence of drusen. Drusen deposits are made up of acellular polymorphous material and typically lie between the retinal pigment epithelium (RPE) and the Bruch's membrane of the retina. There are two varieties of AMD, dry AMD and wet AMD. An individual affected by the dry form exhibits drusen deposits in the macula. The dry form corresponds to the abundance of drusen and may or may not extend to the center of the macula. The wet form corresponds to the neovascularization of the choroid. Using an ophthalmoscope, drusen deposits that form posterior to the retina can be seen when they are greater than 25um in diameter(Jager, Mieler, and Miller, 2005). Only $10-15\%$ of AMD is of the wet form, however this neovascular AMD is responsible for 80% of severe loss of vision. Neovascularization is characterized by abnormal blood vessels growing from the choroid that leak into the retina and cause central vision loss.

1.2 Photodynamic Therapy

Photodynamic therapy (PDT) is a treatment which utilizes light and a photosensitive drug to produce radical oxygen molecules which kill nearby cells. The most common application is for the destruction of cancerous tumour cells in humans however, PDT can also be used to treat AMD. PDT works by injecting a photosensitizer (PS) into the patient, allowing the drug to accumulate in the diseased area, and then focusing a specific wavelength of light onto the area. The light excites the drug, initiating a desired photochemical reaction which is most effective where there is maximum uptake of the drug, in areas where cells are replicating most rapidly. Figure 1.1 shows the excitation and decay of the PS. The PS absorbs the energy via laser light at a corresponding wavelength and is excited into the ${}^1PS^*$ state or the ${}^3PS^*$ state. There are multiple types of reactions that can occur once the PS is activated via light. The PS can be excited from the ground state to a higher energy state and return to the ground state by emitting energy in the form of fluorescence or undergo two types of reactions, Type 1 (oxygen-independent) or Type 2 (oxygen-dependent). In the case of Type 1, the PS reacts with surrounding molecules and produces hyrdoxyl and superoxide radicals. In Type 2 reactions, the excited PS molecules react with molecular oxygen and produce highly reactive singlet oxygen. This singlet oxygen is the main agent that causes cell death via apoptosis or necrosis (Khurana, 2010). Type 2 reactions are thought to be the main cause of cellular damage in PDT.

The method of PS excitation is independent of the reaction type, and therefore the PS can absorb energy via one-photon (OPE) or two-photon excitation(TPE). One photon

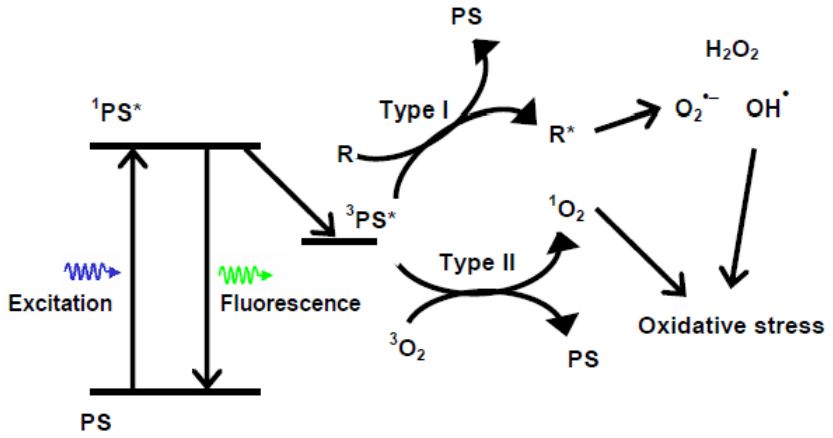

Figure 1.1: The Jablonski diagram of photodynamic therapy. The photosensitizer (PS) absorbs energy at its absorption maxima and is excited to the singlet state $^1PS^*$. This energy can either be released in the form of fluorescence or another state change to $^3PS^*$ through electron flip. The PS undergoes either Type 1 or Type 2 reactions resulting in reactive oxygen species that can result in cell death. The diagram is courtesy of Mamta Khurana. (Khurana, 2010)

excitation, as shown in figure 1.1, occurs when energy corresponding to the difference of the ground state and excited state is absorbed by the PS. TPE is the process when two photons are absorbed simultaneously and are each half the energy (double the wavelength) of the one photon excitation energy. Both the OPE and TPE process are illustrated in figure 1.2. The blue arrow represents OPE from the ground state to the excited state and the red arrow shows excitation to a virtual state which represents the first photon, and a photon excites from the virtual state to the excited state. The probability of the two photon event occurring is proportional to the square of the intensity of light(Ira Probodh, 2012) as shown in equation 1.1, in comparison OPE is linearly dependent on intensity. Therefore a femtosecond laser source is required to increase the probability of a TPE event.

$$\frac{P_2}{P_1} = \frac{\sigma_{2p} I}{2\sigma_{1p}} \tag{1.1}$$

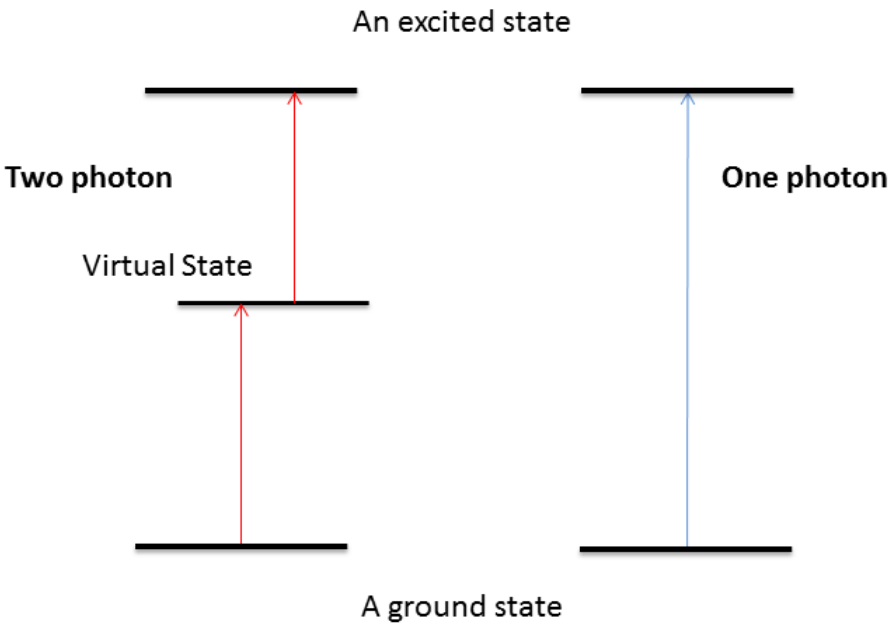

Figure 1.2: On the left is the excitation from a ground state to an excited state via two-photon absorption. The light is absorbed by the photosensitive drug and excited temporarily to a virtual state, then absorbs a second photon to an excited state. The right shows one photon excitation from the ground state to an excited state.

P_1 is the probability of OPE and P_2 is the probability of TPE, σ_{1p} is the one-photon cross section in units of cm^2 and σ_{2p} is the two-photon cross section of the photosensitizer in units of Goeppart-Mayers (GM) where 1 GM is $10^{-50}\ cm^4 * s * photon^{-1}$, and I is the instantaneous laser intensity in units of W/cm^2. The relative probability is per unit area of the drug illuminated. The benefit of the squared intensity dependence means a smaller three-dimensional localization of excitation in the diseased area compared to OPE-PDT. The limited area of excitation means surrounding tissue will be safe from unwanted drug activation in healthy tissue (Mamta Khurana and Wilson, 2012).

Verteporfin (Visudyne) is the one-photon drug used in excitation PDT that slows down the progression of AMD. A study showed that patients with choroidal neovascu-

larization (CNV) due to AMD benefit from the one-photon photodynamic therapy (OPE-PDT)(Hooper and Guymer, 2003). The use of one-photon excitation is limited because the PS is excited along the entire path of light incident on the diseased area causing new blood vessels to grow in that region that leak into the retina causing damage. The damage to the unwanted areas up-regulates the Vascular Endothelial Growth Factor (VEGF) which signals protein to restore oxygen supply to the treated area via vascularization. Verteporfin PDT must be repeated every 3-4 months because of revascularization, which is thought to be a result of the damage to healthy tissue during the treatment(Hooper and Guymer, 2003). In the Kaiser et al paper, Verteporfin was shown to reduce the risk of severe vision loss however there was no vision improvement after treatment. In contrast, injection treatments of anti-VEGF antibody's have demonstrated vision improvement in AMD separate from Verteporfin treatment. Ranibizumab, an antibody that binds with VEGF isoforms showed increases in visual acuity when used alone and Bevacizumab an anti-VEGF antibody also showed vision improvements for treatment of CNV (Kaiser, 2009). More recently Verteporfin was shown to improve the visual acuity when combined with these anti-VEGF antibodies.

A new family of photosensitizer drugs were developed specifically to obtain a good TPE cross section (Khurana, 2010). A TPE drug made from conjugated porphyrin dimers were shown to have a maximum TPE cross section of 17,000 GM in comparison to Verterporfin (50GM) and have high singlet oxygen quantum yields, making it a potential drug for TPE-PDT (Hazel A. Collins, 2008). More recently, successful *in vivo* TPE blood vessel closure was demonstrated in a window chamber mouse (WCM) model for 40 micron diameter blood

vessels using infrared light (λ = 920nm). The next phase of TPE-PDT is to demonstrate blood vessel closure *in vivo* in an eye model (Khurana, 2010).

In the past, the rat has been used for biomedical research and in particular has been shown to be a great model for treatment of AMD. Compared to other model choices such as the mouse and rabbit model, the rat eye was used by Bird because of the low f-number of the eye lends itself to the success of TPE. The f-number of the rat eye is half the f-number of the objective lens used in the WCM model and may result in better TPE-PDT efficacy (Bird, 2006, Khurana, 2010). Unfortunately, the optical aberrations of rat eye reduce retinal image quality and consequently reduce the probability of TPE. These optical aberrations present in the rat eye can be reduced with the use of adaptive optics (AO) and a Hartmann-Shack wavefront sensor.

1.3 Overview

It was my goal to design an apparatus to deliver a light dose to the retina in a rat model using adaptive optics. The demonstration of blood vessel occlusion in an animal model is the next step towards the feasibility of TPE-PDT for treatment of AMD. The main objective was to correct the wavefront aberrations caused by the optics of the eye to improve the probability of the TPE.

The following is an outline of this thesis which describes the progress of the project for TPE-PDT treament of AMD. In chapter 2, the design and modification of the Waterloo CSLO with the addition of AO and a Hartmann-Shack wavefront sensor is outlined. A description of integrating the Xinetics 37-channel deformable mirror and the challenges

associated with creating a diffraction-limited system suitable for TPE-PDT are presented. An analysis of the optical components in the system that contribute significant aberrations and minimization of their contributions is provided. In chapter 3, retinal images and wavefront measurements using the AOSLO on Long Evans rats with rigid contact lenses and spectacle lens correction before and after wavefront correction with a Xinetics 37-channel deformable mirror are reported. In chapter 4, I will extend the schematic rat eye model (M.C.W. Campbell, 1981) with the addition of a contact lens and spectacle lens. It is shown that the contact lens introduces defocus and spherical aberration that is dependent on the radii of curvature of the contact lens. The tear lens between the contact lens and the eye also has a significant impact on the nominal power of the contact lens. I will demonstrate that the combination of the rigid contact lens and spectacle lens correction can improve retinal image quality and therefore the probability of TPE-PDT prior to adaptive optics correction. Finally, in chapter 5, an assessment of the apparatus and rat holder is discussed to improve the repeatability of experimental conditions. Some recommended design changes are suggested to improve future wavefront sensing and imaging capabilities of the rat eye for the success of *in vivo* TPE-PDT in the rat eye.

Chapter 2

Two Photon Excitation Delivery Apparatus

In this chapter the design of the Waterloo Adaptive Optics Confocal Scanning Laser Ophthalmoscope (AO-CSLO) is outlined. My goal was to take the existing system and integrate a Hartmann-Shack (H-S) wavefront sensor and a Xinetics 47mm aperture deformable mirror. The following system utilizes three lasers at wavelengths: 633nm for imaging, 830nm as a beacon for the wavefront sensor and a 920nm femtosecond laser source for two-photon excitation. The imaging arm creates a raster scan across the retina to image retinal features, the sensing arm is a non-scanning beam which allows for the measurement of wavefront aberration of the eye and the treatment arm, which follows the optical path of the H-S arm, allows activation of a photosensitive drug in the retina with an adaptive optics corrected beam. All three lasers reflect off the Xinetics deformable mirror to allow for real-time correction of the wavefront aberration of the eye. Prior to building the optical system we modelled the apparatus in Zemax, an optical design software, to determine and minimize the optical aberrations.

We required the optical apparatus to be diffraction-limited as defined by the Maréchal criterion (the RMS wavefront aberration is less than $\lambda/14$ and a Strehl ratio of at least 0.8

(Hecht, 2002)) so the aberrations of the system are negligible relative to the aberrations of the rat eye. This is important to maximize the image quality which is also an indication that the light going into the eye is focussed to a localized volume which is necessary for successful two photon excitation. The minimization of system aberrations also reduces the demand on the adaptive optics mirror to correct the aberrations of both the eye and system.

2.1 Wavefront Measurement

The Hartmann-Shack (HS) sensor used in the Adaptive Optics Confocal Scanning Laser Ophthalmoscope(AOCSLO) was used to measure the wavefront aberrations of the eye similar to the use of a HS used to measure a human eye. We need to measure the aberrations of the rat eye to operate a deformable mirror and correct the aberrations in real time. Correction of the aberrations is very important to ensure a tight localized focal volume for two photon excitation. In the next three sections below, I describe the theory of a Hartmann-Shack wavefront sensor used in our AOSLO.

2.2 Theory of Hartmann-Shack Wavefront Sensor

The Hartmann Shack (HS) wavefront sensor is a device used to measure wavefront aberrations. Ingoing light is focused by the optics of the eye onto the retina and diffusely scattered back out of the eye. The emerging beam from the eye is relayed through telescopes to a lenslet array, which is conjugate to the pupil plane, and is focused onto a CCD camera. The wavefront is transversely magnified through the relay telescopes and the local slope

is sampled by the lenslet array. The HS measures the shape of the wavefront relative to a planar reference wavefront. Ideally the wavefront is planar so the spots across the pupil are imaged to the optical axes of their respective lenslets. In figure 2.1, a cross section of the lenslet array shows a planar wavefront focussed to the CCD plane. The planar wavefront focusses through each lenslet to give focal spots on their respective optical axes. However, in an aberrated wavefront (figure 2.2) the spots shift relative to the reference positions in 2.1. The spacing of the spots is defined by the lenslet pitch (lenslet diameter) and the deviations from the reference spots vary proportional to the local slope of the wavefront error. The shifts are related to the derivatives of the wavefront aberrations in both the x and y directions:

$$\Delta x = \frac{-f dW(x,y)}{dx} \tag{2.1}$$

$$\Delta y = \frac{-f dW(x,y)}{dy} \tag{2.2}$$

where f denotes the focal length of the lenslet array and $W(x,y)$ the wavefront aberration. From the local slopes across the pupil the wavefront aberration can be extracted using a least squares method Cubalchini (1979) . From equations (2.1) and (2.2) a least squares method can be constructed of the form

$$A = (DD^{-1})DP \tag{2.3}$$

where the directional slope shifts (P), the coefficients of the Zernike polynomials (A),

and the matrix of derivatives of the Zernike polynomials at the corresponding spot locations (D) are used. D^{-1} denotes the inverse of the matrix, D. The Zernike polynomials are a set of orthogonal functions that describe wavefront aberrations and will be discussed in more detail below.

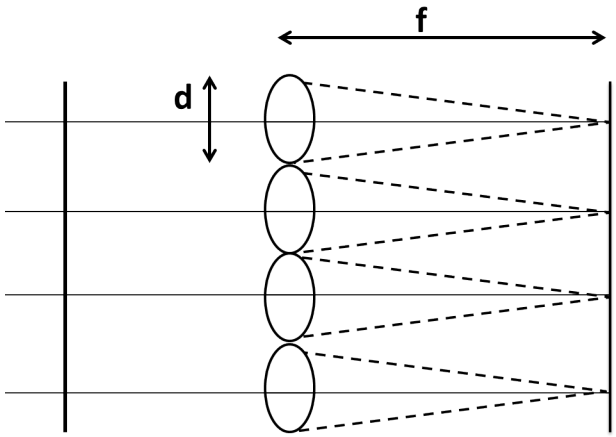

Figure 2.1: A cross section shows a planar wavefront incident on the Lenslet Array (LA). The LA focusses spots to the focal point of the lenslets and the spots lay on the lenslet optical axes in their reference positions.

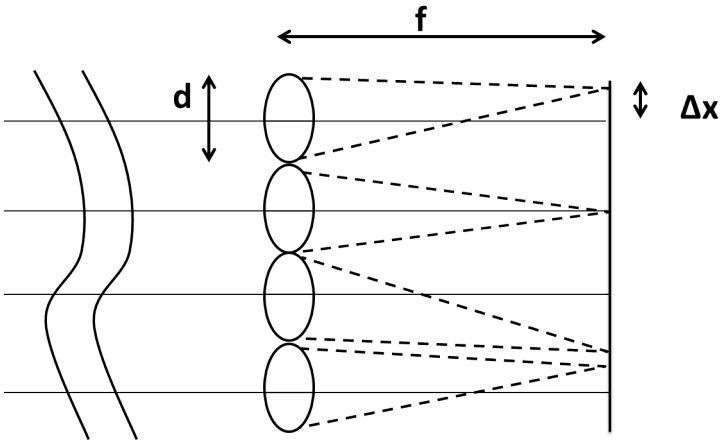

Figure 2.2: A cross section shows an aberrated wavefront incident on the LA. The LA samples the local slope of the wavefront and the spots are deviated from the reference positions.

2.3 Dynamic Range and Sensitivity

There exists a trade off between dynamic range (maximum wavefront aberration that can be measured) and the sensitivity of the HS wavefront sensor due to the parameters of the lenslet array as well as the centroiding algorithm. The software used to centroid the spots is also limited by the spot quality produced by the lenslet array. Therefore if the the spot quality is poor (very blurry) the measurement made by the centroid algorithm will not be accurate. Assuming sufficient spot quality then the dynamic range is limited by the largest amount a spot can move without crossing over into another lenslet aperture. The maximum angle through which a spot can move is defined below:

$$\theta_{max} = \frac{\Delta d_{max}}{f} = \frac{s/2}{f} \tag{2.4}$$

Δd_{max} is the maximum deviation of the spot on the CCD, s is the lenslet diameter and f is the focal length of the lenslet array. The spot can only move one-half of the aperture of the lenslet array before it would crossover into the area of another spot(Geunyoung Yoon, 2004). In reality the deviation is less than in equation 2.4 because the spot has a minimum spot size defined by the diffraction limit of the lenslet. The minimum deviation is defined by the smallest increment the sensor can measure and so is defined by the pixel size of the CCD camera. So similarly, using 2.4 above, the minimum angle a spot can move is defined as:

$$\theta_{min} = \frac{\Delta d_{min}}{f} = 2\frac{CCD_{pixel}\theta_{max}}{s} \tag{2.5}$$

where CCD_{pixel} is the pixel size of the CCD camera used in the wavefront sensor. Substituting equation 2.4 into 2.5 for focal length we can see the minimum angle a spot can move is linear with the maximum angle the spot can move. More dynamic range comes at the cost of system sensitivity because the spot needs to move by CCD_{pixel} to be detected. The choice of the lenslet focal length and lenslet apertures depend on the eye model being measured. For example, the rat eye has a significant amount of defocus and having a large dynamic range would be necessary to measure the wavefront aberration compared to the human eye which tends to have smaller wavefront aberrations. Choosing a lenslet to be more sensitive at the cost of dynamic range does not affect measuring the human eye. There are methods to help improve the dynamic range while maintaining the sensitivity, but they are outside the scope of this project.

2.4 Wavefront and Zernike Polynomials

Using ray optics to describe a light path, a wavefront is the surface perpendicular to rays of light originating from a point source. In an optical system without aberrations, the surface emanating from a point source is a sphere and the further from the point source, the wavefront becomes planar. In reality, optical systems are affected by aberrations and all of the rays corresponding to the wavefront will not focus to a point. Wavefronts are distorted in the longitudinal directions. The wavefront aberration is the difference between the measured wavefront and a reference sphere. Wavefront aberrations can be described using the Zernike polynomials which form an orthogonal set of functions. The wavefront

aberrations can be expanded in the form below:

$$W(\rho,\theta) = \sum_{n}\sum_{m} C_n^m N_n^m Z_n^m(\rho,\theta) \tag{2.6}$$

where ρ is the radial distance from the center of the pupil, and θ is the angle measured from the horizontal axis with the z-axis coming out of the eye.

The Zernike polynomials are used to represent wavefront aberrations because they are an orthogonal set which represent different types of known aberrations, such as defocus, coma and astigmatism. They are normalized over the pupil of the eye using Noll's constants (N_n^m), and the coefficients (C_n^m) represent the contribution of each aberration. It is worth noting here that the derivatives are not orthogonal (Cubalchini, 1979) and cause Zernike terms to be cross-correlated when extracting wavefront aberration from HS spot patterns. The Zernike polynomials are useful in the reconstruction of the wavefront, as well as used to calculate the point spread function (PSF) and other image quality metrics.

The Zernike polynomials are presented in a double indexing scheme given in the form

$$Z_n^m(\rho,\theta) = R_n^{|m|}(\rho,\theta)cos(m\theta) \quad \text{for m} \geq 0 \tag{2.7}$$

$$Z_n^m(\rho,\theta) = -R_n^{|m|}(\rho,\theta)sin(m\theta) \quad \text{for m} < 0 \tag{2.8}$$

where $R_n^{|m|}$ is the dependence of each polynomial on ρ and θ. Using the Zernike polynomials the wavefront can be broken up into independent orthogonal terms, and the higher

order aberrations can be measured. When the amount of aberration is reported, the average absolute root-mean-square (RMS) wavefront error of the Zernike polynomials is used. According to the Optical Society of America (OSA) conventions, each term is normalized to have a unit variance, and therefore when a wavefront aberration is scaled by an aberration coefficient, the variance is equal to the square of the aberration coefficient. The RMS of each term has the units of microns or waves.

By convention the wavefront error is equal to zero at the center of the pupil and the wavefront aberration is written as a sum of the Zernike polynomials as in equation 2.6. When $W(x, y)$ is positive the wavefront aberration exiting the eye is said to be phase-advanced and when negative to be phase-lagged. The RMS wavefront error can be calculated from the sum of the squares of the aberration coefficients:

$$RMS = \sqrt{\sum (c_n^m)^2} \tag{2.9}$$

The RMS wavefront error across the pupil is therefore an image quality metric of the eye relative to the perfect case when the RMS is equal to zero. The larger the RMS wavefront error, the more degraded the image quality.

In table 2.1 the Zernike terms are listed in two indexing schemes, in polar form with their associated names up to fourth order. Usually the piston term is not included in the RMS wavefront error because the variance of the Zernike term is not equal to one. The piston term is a constant offset with no slope and therefore cannot be measured by a conventional HS apparatus.

Table 2.1: Zernike terms up to fourth order and their names and index. The wavefront errors can be fitted above fourth order, in this thesis they were fitted to 7th order.

#	n	m	Z_n^m	N_n^m	Polar Form	Name
0	0	0	Z_0^0	1	1	Piston
1	1	-1	Z_1^{-1}	2	$rsin\theta$	Tip
2	1	1	Z_1^1	2	$rcos\theta$	Tilt
3	2	-2	Z_2^{-2}	$\sqrt{6}$	$r^2sin2\theta$	Oblique Astigmatism
4	2	0	Z_2^0	$\sqrt{3}$	$2r^2-1$	Defocus
5	2	2	Z_2^2	$\sqrt{6}$	$r^2cos2\theta$	Vertical Astigmatism
6	3	-3	Z_3^{-3}	$2\sqrt{2}$	$r^3sin3\theta$	Vertical Trefoil
7	3	-1	Z_3^{-1}	$2\sqrt{2}$	$(r^3-2r)sin(\theta)$	Vertical Coma
8	3	1	Z_3^1	$2\sqrt{2}$	$(r^3-2r)cos(\theta)$	Horizontal Coma
9	3	3	Z_3^3	$2\sqrt{2}$	$r^3cos3\theta$	Oblique Trefoil
10	4	-4	Z_4^{-4}	$\sqrt{10}$	$r^4sin4\theta$	Oblique Quadrafoil
11	4	-2	Z_4^{-2}	$\sqrt{10}$	$(4r^4-3r^2)sin(\theta)$	Oblique Secondary Astigmatism
12	4	0	Z_4^0	$\sqrt{5}$	$6r^4-6r^2+1$	Spherical Aberration
13	4	2	Z_4^2	$\sqrt{10}$	$(4r^4-3r^2)cos(\theta)$	Vertical Secondary Astigmatism
14	4	4	Z_4^4	$\sqrt{10}$	$r^4cos4\theta$	Vertical Quadrafoil

2.5 Retinal imaging with adaptive optics

Adaptive optics is a technique used to improve an optical system by compensating for wavefront error due to aberrations produced by an optical system. The technique is used in astronomical telescopes to correct for atmospheric distortions while imaging stars as well as in vision science for the correction of aberrations of the eye for retinal imaging. Specifically for adaptive optics in vision science and retinal imaging, the aberrations of the eye and the diffraction generated by the pupil size limit the ability to resolve retinal features(Nathan Dolbe, 2006). In conventional use, spectacle lenses or contact lenses are used to correct astigmatism and defocus which correspond to the low order Zernike aberrations. However, adaptive optics can correct both low order and high order aberrations corresponding to the Zernike polynomials in table 2.1. Adaptive optics works by measuring

the wavefront aberrations using a Hartmann-Shack setup and compensating for them by using a deformable mirror.

Figure 2.3 shows a general path diagram of an adaptive optics system to improve retinal images using a deformable mirror. The diagram shows the path of the light going into the eye (blue) and leaving from the eye (red). The wavefront emanating from the eye is distorted due to the optical aberrations of the eye and is sent through relay optics (scanning optics and telescopes) and then incident on a deformable mirror (DM). The DM "corrects" the shape from distorted wavefront to planar wavefront after reflection (improving spot quality). The light is then split via a beam splitter (BS) where it is measured via a Hartmann-Shack (HS) wavefront sensor, which controls the DM, and collected by an imaging sensor. The improvement of the shape of the wavefront allows the outgoing light to be focussed more sharply onto an imaging sensor which improves the image quality. Due to the property of light reversal, light going into the system (blue) and reflected onto the DM allows for improvement of the light focussed onto the retina of the eye. The improved point spread function on the retina allows for higher peak intensity on the retina and higher resolution and contrast in retinal images. Correction of the wavefront on the outgoing path further improves the resolution and contrast in retinal images.

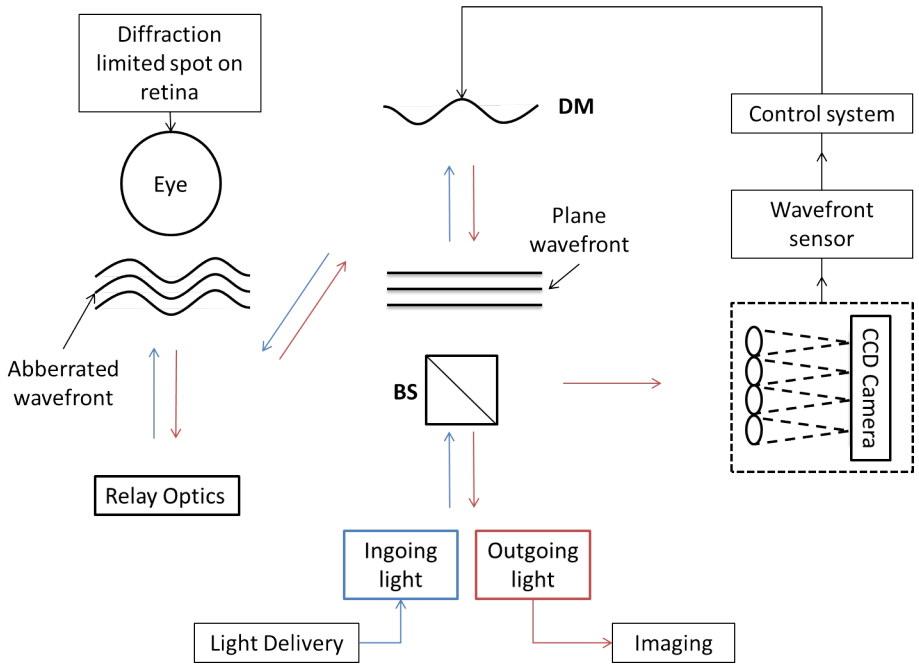

Figure 2.3: A path diagram of how adaptive optics is used for light delivery and improved image resolution. In this diagram the planar ingoing light (blue) goes through a beam splitter (BS) and is reflected off a deformable mirror (DM), where it takes the shape of the DM, then through relay optics and into the eye where it is focussed to a diffraction-limited spot. The light emanating from the eye, (red) exits with an aberrated wavefront corresponding to the aberrations of the eye. After reflection off the DM, the wavefront becomes planar where it splits to the wavefront sensor and imaging sensor. The wavefront sensor measures the shape of the wavefront and controls the DM through a closed loop control system. The treatment beam follows the ingoing (blue) path to benefit from the AO correction to improve TPE probability.

2.6 Wavefront corrector: Xinetics 37-actuator deformable mirror

The Xinetics deformable mirror has 37-PMN electroceramic actuators with a maximum stroke of 4um and a 47mm aperture. The mirror uses a thin-film continuous sheet of silvered mirror as the reflective surface. The discrete actuators are able to push and pull the mirror surface to deform a reflected wavefront for aberration correction. The mirror is capable of correcting higher order aberrations of the eye. Although this particular

deformable mirror has been shown to correct higher order aberrations in other AO systems (Nathan Dolbe, 2006), the large 47mm aperture requires very long optical path lengths to magnify the pupil and take full advantage of the deformable mirror. The smaller 4um stroke also limits the dynamic range and therefore even large second order aberrations like defocus and astigmatism may take up the full stroke, leaving little correction for any higher order terms. To conserve the stroke of the mirror, sphere and cylindrical lenses have to be used to correct the eye.

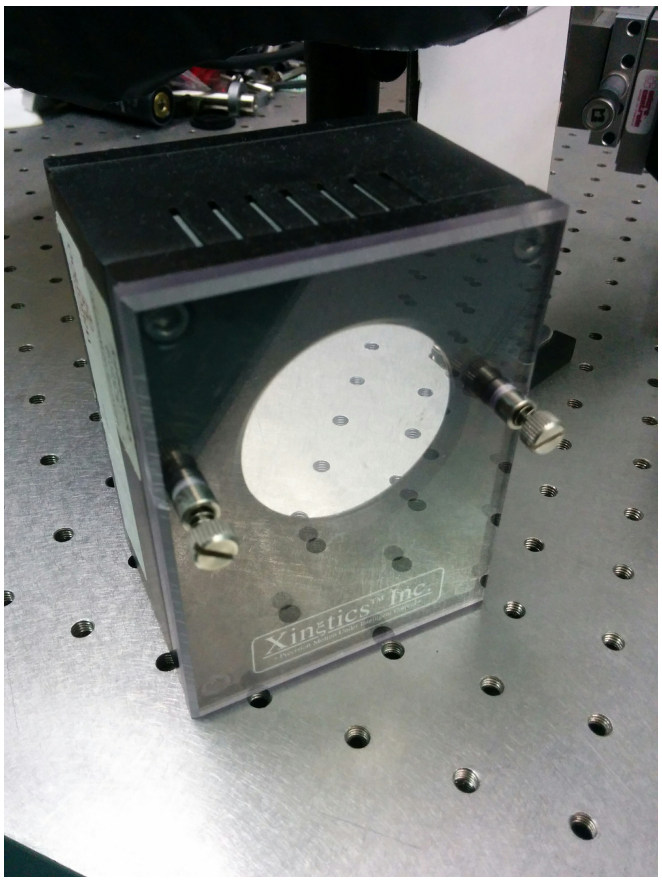

Figure 2.4: The Xinetics 37 actuator 47mm deformable mirror. The mirror is controlled by a MUX driver which delivers serial commands for each actuator. In this picture we can see the large aperture of the mirror.

2.7 Adaptive optics correction of the rat eye

The rat eye was specifically chosen as a model of age-related macular degeneration for this project. Theoretically the lower f-number of the rat eye should provide higher resolution images, as compared to images of the human eye (Xiaolin Zhou and Metha, 2012). However, images of the rat retina have been observed to be of poorer quality than human retinal images due to the large aberrations of the rat eye. It has been suggested that AO correction could be used to correct these aberrations. AO retinal images have been successfully captured but none so far have achieved the diffraction-limit of the rat eye. The challenges associated with achieving well corrected AO images of rodent eyes have been attributed to the aberrations varying through the depth of the retina (Ying Geng and Porter, 2009). However, it was shown by Mark Bird when modelling the optics of the rat eye, that the aberrations do not change with defocus and only a defocus value is required to optically slice through the retina (Bird, 2006). This is important because the rodent eye is much thicker optically, 11D (A. Chaudhuri, 1982, M.C.W. Campbell, 1981) compared to a 0.7D thick human retina.

Some attempts have been made to improve imaging and wavefront sensing of the rodent eye by utilizing a fundus lens to neutralize the refraction of the cornea of the rat eye (Y. Jian, 2013). A fundus lens increases the focal length, thus increasing the f-number and reducing the potential resolution gain between the rodent and human eye. Although this might help with wavefront sensing it reduces the potential image quality as well as the probability of the TPE in the eye (Bird, 2006). Geng used an annular wavefront beacon

to remove light scattered from varying layers in the retina. According to this work, spot quality of the HS pattern is poor due to many reflections of the beacon from multiple layers in the mouse retina(Geng Y, 2012). They describe the phenomenon as similar to the elongation of spots from using guide stars in astronomy. In the case of the mouse eye, the thickness of the retina is postulated as the cause of elongated spots. To reduce the depth of focus they used the largest beam possible of 2mm to fill the pupil. (3um depth of focus for diffraction limited mouse eye, 2mm pupil, NA = 0.49). To avoid back reflections from the cornea, and possibly the posterior surface of the lens, an annular beacon of 0.3mm inner diameter was used. Then the beacon was focused on the retinal layer of interest, and due to the small depth of focus the elongation of the HS spots were reduced.

The wavefront sensor is essential in the control loop for real time adaptive optics. The HS beacon enters the eye which then scatters back to the wavefront sensor. Typically in a HS system the beacon is non-scanning, however, when used in conjunction with a CSLO, the beam may be scanning. A non-scanning beam measures the aberrations from a spot on the retina. In contrast, the scanning beam measures the aberrations over a small patch and averages the aberrations of the eye over that patch of the retina. In this research project, the quality of the wavefront sensor spots and correction is most important at the point of focus of the treatment beam, so the beam was chosen to be non-scanning. The quality of correction directly correlates with the light dosage on the retina for TPE.

2.8 Apparatus design

The following is a description of the CSLO, HS and treatment components of the apparatus used for this research, beginning with each laser source through each optic and ending at the eye and/or corresponding detector. Laser intensity used in this system were calculated to be within the maximum possible exposure defined by the American National Standards Institute for eye safety.

2.8.1 Confocal scanning laser ophthalmoscope (CSLO)

The laser source of the CSLO is a Helium-Neon (HeNe) source with a wavelength of 632.8nm, as shown in figure 2.5. The laser beam first passes through a neutral density filter to attenuate the power at the eye to prevent oversaturation and damage to the retina. The CSLO beam then passes through an entrance pinhole which controls the beam diameter at the rodent eye. The entrance pinhole is conjugate to the eye's pupil. The entrance pinhole is located at the focal length of the first telescope with a magnification of 3.33x. The beam is then expanded and propagates through two dichroic plates. The first dichroic plate is a low pass at 700nm to allow for reflection of the 830nm HS beam, on the second pass from the subject's eye to the lenslet array of the Hartmann-Shack wavefront sensor. The second dichroic is another low pass filter at 870nm to allow for the reflection of the treatment beam at 920nm into the system. The CSLO beam then propagates to a second telescope with a magnification of 21.16x to magnify the laser sources to fill a 42mm aperture Xinetics Deformable Mirror. The light then propagates back through another reverse 21.16x telescope (shown as dashed box) and is incident on another dichroic low pass

at 700nm to reflect the 830nm and 920nm beams to a set of telescopes to propagate to the subject's eye. The CSLO imaging beam continues through a telescope with magnification of 0.45x and is incident on a 25 facet polygon mirror.

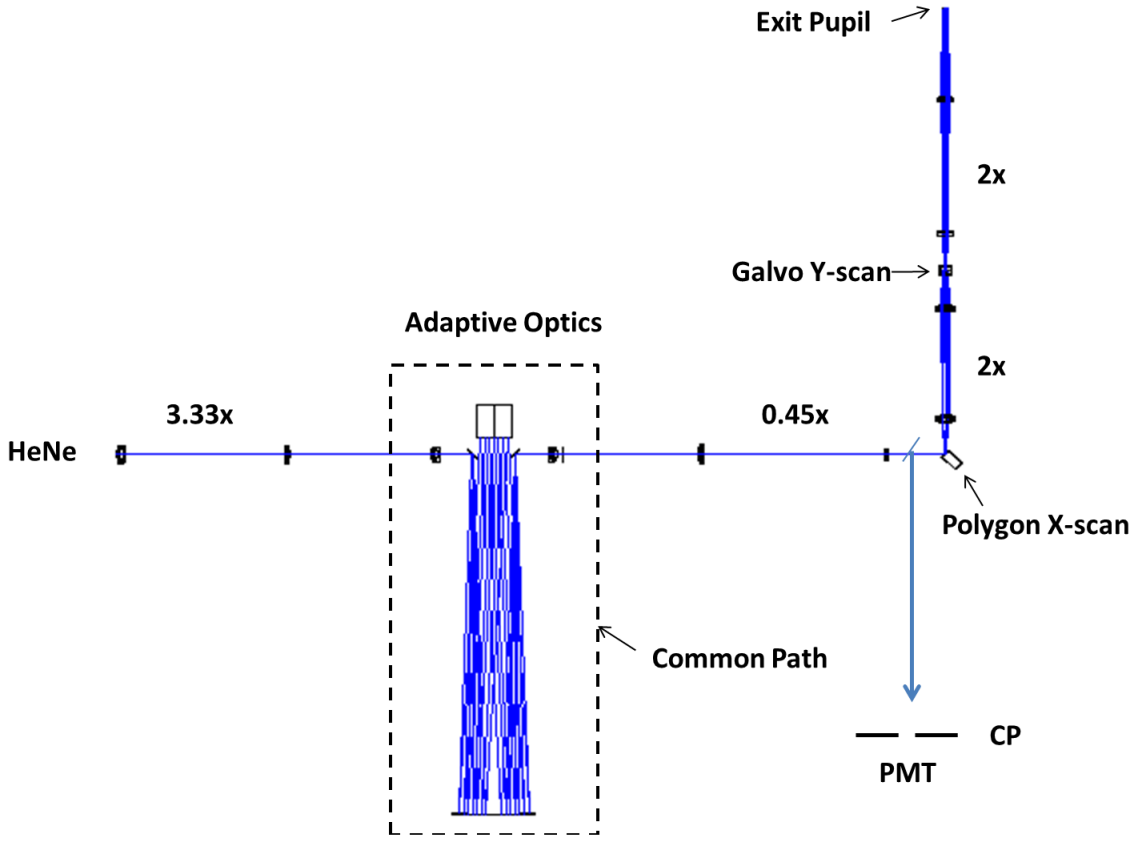

Figure 2.5: A ray diagram showing the Waterloo confocal scanning laser ophthamoscope. The first scanning optic is a polygon mirror that rotates a 25 facet mirror at 614 revolutions per second. The second scanning optic is a galvanometer mirror which vibrates about a central angle. The scanning optics pivot the light in the pupil plane to create a raster scan across the retina. The light scatters out of the eye and back to the photomultiplier tube to create an image. Note the exit pupil of the system is aligned with the entrance pupil of the rat eye to image the retina.

The polygon mirror is rotating at 614 revolutions per second and scans the beam horizontally through 28.8 degrees, although only 20 degrees is used to ignore vignetting of the light on the edges of the facets. The reflected light travels through a 2x beam expander,

decreasing the scan angle by 50%. A mirror positioned behind this telescope reflects the scanning beam upwards by 90 degrees to a galvanometer mirror. The galvanometer mirror scans the beam vertically creating a raster scan. The entire scan then propagates through another 2x expander reducing the scan to a 5 degree field. The CSLO passes then passes through a low pass dichroic at 700nm to allow the beacon and treatment beam to combine with the imaging beam. Finally the beam passes through a trial lens chosen specifically to correct the subject's refractive error. The exit pupil of the AOSLO system is aligned with entrance pupil of the subject's eye. When the scanning beam reflects back the light is descanned and incident on the beam splitter where it is reflected onto a lens and focussed onto a confocal pinhole (CP). The pinhole is located at the focal point of the lens and is conjugate to the retina of the eye. The pinhole restricts scattered light from layers positioned axially away from the focussed light and creates the ability to optically section axially through the retina. The light then enters a photomultiplier tube (PMT) where it is detected and images at 30 frames per second are processed by the computer and sent to a monitor and hard drive for recording.

2.8.2 Hartmann-Shack (HS) wavefront sensor

The laser source for the HS wavefront sensor is a Thorlabs fiber coupled laser diode with a wavelength of 830nm, as shown in figure 2.6 . The laser source first is collimated using an objective lens. The beam goes through a neutral density filter to attenuate the power at the eye. The beam then goes through a pinhole located at the first focal point of a 2x expander, which defines the pupil size. A 50 : 50 beam splitter lies between the pinhole

and first lens (to allow light to reflect back on the second pass to the deformable mirror and wavefront sensor). The beam transmits through the beam splitter then reflects off of a 45 degree 700nm low pass dichroic into the rodent or subject's eye. The subject's pupil is coincident with the exit pupil of the instrument which lies at the second focal length of the telescope, conjugate to the pinhole. The light reflects out of the eye, through the telescope and reflects off the beam splitter and through two relay telescopes of total magnification of 1.11x. The light then reflects into the adaptive optics telescope via another 45 degree 700nm low pass dichroic. Then the beam enters a set of telescopes common with the CSLO with magnification 21.16x (from section 2.8.1), onto the Xinetics deformable mirror. The light exits and reflects out of the CSLO system path telescopes via another dichroic and through a 2x telescope to make a final pupil size of 7mm on the CCD. At the second focal length of the telescope, a lenslet array with focal length of 18mm samples the wavefront and focusses onto a PCO CCD Camera. The camera relays the Hartmann-Shack spots to the monitor and they are processed using Miniwave (from University of Rochester) to determine the wavefront aberrations of the rat eye and the system.

2.8.3 Treatment beam

The laser source for the treatment beam is a tunable Chameleon Ultra II femtosecond laser source with a wavelength at 920nm. The beam enters the CSLO and HS system path via a 90 degree 700nm low pass dichoric before the adaptive optics telescopes, a shown in figure 2.6. The light is incident on the Xinetics deformable mirror and follows the optical path of the HS onto the eye. The treatment beam was chosen to be non-scanning because we

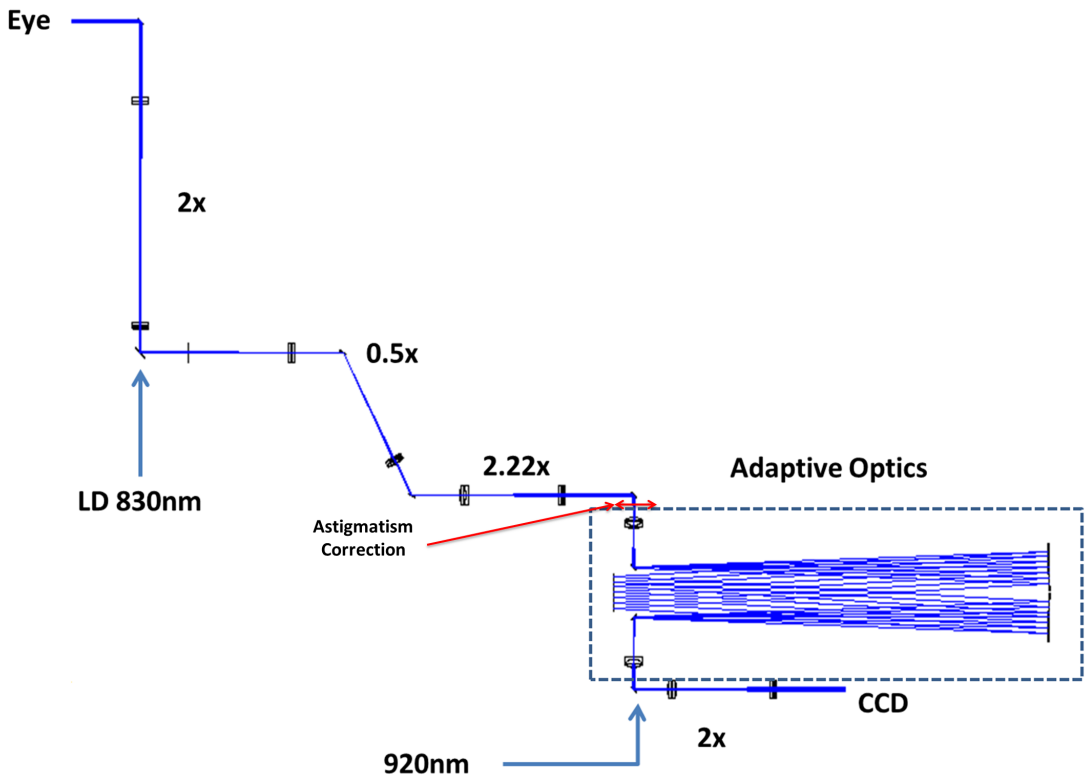

Figure 2.6: Hartmann-Shack and treatment beam layout shows the light from the laser entering the eye. It then reflects back out of the eye to the CCD camera. The path shows the multiple relay telescopes to magnify the 3.5mm pupil to the 47mm Xinetics Deformable mirror and back to a 7mm pupil at the CCD camera. Using the astigmatism correction to compensate for the induced astigmatism of the spherical mirrors we attained a diffraction limited system. The 920nm treatment beam enters the system via a dichroic and follows the reverse path of the HS to the eye.

intend to isolate one vessel for TPE treatment.

2.9 Design Specifications, Constraints and Improvements

The design constraints of combining the CSLO, Xinetics deformable mirror and Hartmann-Shack wavefront sensor were defined by an existing CSLO, the aperture of the Xineteics deformable mirror and the rat eye entrance pupil. The pupil must be magnified to the aperture of the Xinetics 37-channel deformable mirror of 47mm and minified to a $3.5mm$ pupil at the rat eye. Due to the large aperture of the deformable mirror a set of symmetric telescopes made up of $f = 30mm$ lenses and $47mm$ aperture $f = 635mm$ gold-coated spherical mirrors were used to magnify the entrance pupil. Creating telescopes containing a spherical mirror presents the problem of astigmatism due to the off-axis nature of the telescope. We opted for an in plane optical apparatus (simpler), for which an astigmatism correction was required using a cylindrical spectacle lens in the system. To get rid of off-axis astigmatism without a spectacle lens, the telescope must be constructed out of plane to add another degree of freedom. Finally, we required a non-scanning wavefront sensor and treatment beam and so the three beams, imaging at 633nm, wavefront sensor at 830nm and the treatment beam at 920nm had a combined, large bandwidth which required the common optical paths of the apparatus to have achromatic lenses.

The second major constraint is to separate the CSLO beam from the Hartmann-Shack laser beacon and the treatment beam. The wavefront sensor beacon was chosen to be non-scanning because the aberrations of the rat eye were expected to change rapidly across the field. The aplanatic patch of the eye being smaller than a human eye would affect wavefront sensing as well as correction of the beacon scanned across the 5 degree field of

view. If the aberrations were to change too rapidly across the field, HS spot blur would increase and this could cause unstable correction from the deformable mirror. Also the femtosecond laser source was to follow the optical path of the HS to deliver the energy required for two-photon excitation. The treatment beam was also non-scanning to isolate the region to one blood vessel instead of activating the drug over the entire field.

A setback that we encountered in our system design was the intensity loss at the two f = 30mm achromatic lenses in the AO telescopes (figure 2.5). The two wide-band achromatic lenses were chosen to propagate all three beams to be coincident on the deformable mirror. Contrary to the manufacturers specifications, we discovered a 7% loss at each surface of these lenses at 633nm, which limited the intensity of light to the detector (PMT). We adjusted the design of the AOSLO as shown in figure 2.5, so the imaging arm was a single pass on the deformable mirror. The disadvantage of this set up was that the retinal images would benefit only from a single pass through the adaptive optics correction before arriving at the detector.

2.9.1 Minimizing the system aberrations due to the integration of the Xinetics deformable mirror

I modelled the two telescopes required to magnify the three beams to the 47mm aperture of the Xinetics deformable mirror. The two afocal telescopes as shown in figure 2.7 A, made up of $f = 30mm$ lenses and $f = 635mm$ gold-coated spherical mirrors which were used to magnify the beam to a 47mm aperture and then minify it. From the Zemax modelling we determined that using the off-axis spherical mirrors introduces astigmatism into the system. We determined that minimizing the angles of the spherical mirrors minimizes the

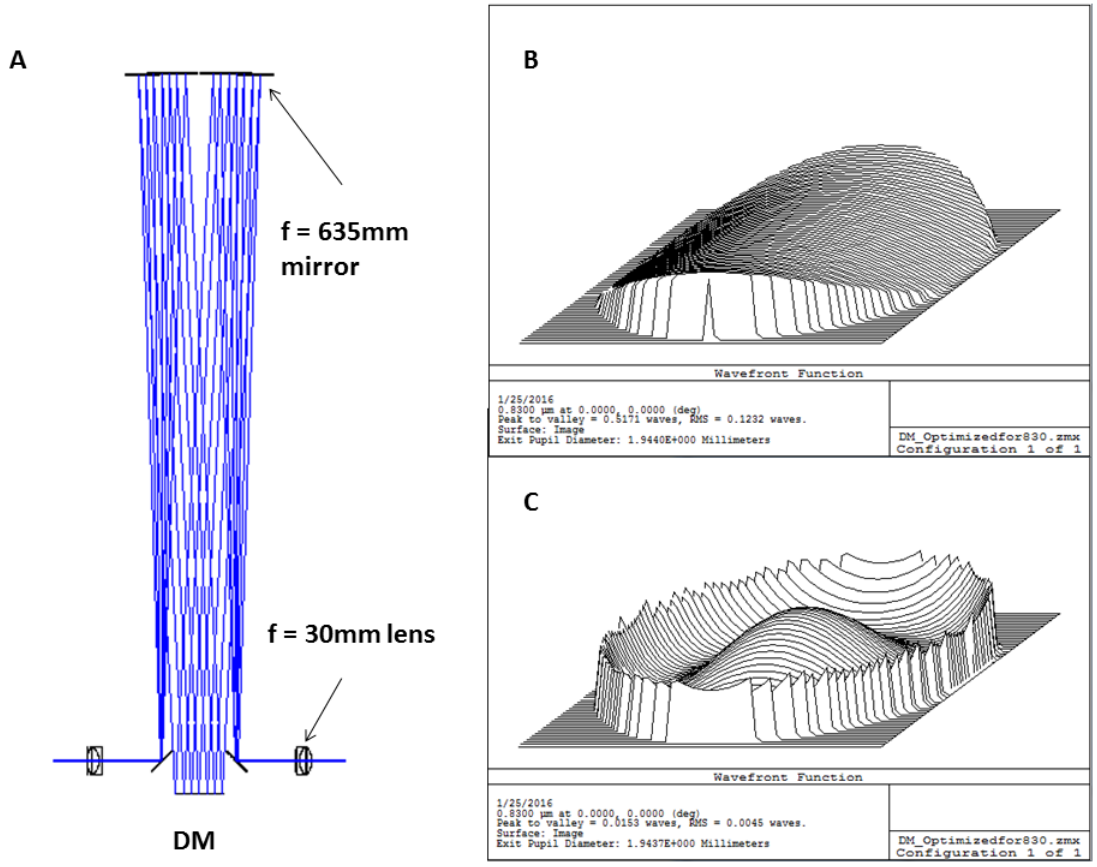

Figure 2.7: A) Layout of the two symmetric telescopes magnifying three beams to the 47mm Xinetics deformable mirror (DM) B) The wavefront shape showing astigmatism induced by the two telescopes (amount in waves) C) The astigmatism corrected using a cylinder correction, left a very small residual defocus (0.0045 waves).

astigmatism. However, an angle of 1.5 degrees of the spherical mirrors was the minimum angle we could rotate the spherical mirrors before the optics would overlap with each other. To minimize the residual aberration (figure 2.7 B) of the telescopes a paraxial XY surface in Zemax was used, where the cylindrical lens power was placed, to correct the astigmatism as shown in 2.7 C.

After correction of the astigmatism due to the off-axis telescopes we had a residual RMS equal to 0.0045 waves which is an acceptable amount of aberration to be considered

diffraction-limited (Maréchal criterion). The aberrations introduced by these telescopes effects all three lasers in the system because they are the only common optical path. Therefore from Zemax we were able to minimize the most significant aberration induced by the system optics.

2.9.2 Verifying that the HS and treatment delivery optical paths are diffraction-limited

As mentioned above the astigmatism of the telescopes for magnifying the light to the 47mm aperture deformable mirror was minimized using a cylinder correction lens. We needed to verify that the aberrations through the entire optical path from the eye to the CCD camera was diffraction-limited to ensure our treatment beam was well corrected at the eye. Similar to the section above, this ensures that the treatment beam will be diffraction-limited entering the eye and means that TPE will depend on our ability to correct the rat eye wavefront aberrations. In figure 2.6 the layout of the HS and treatment beam optical paths from the eye to the CCD camera through a series of relay telescopes (described in section 2.8.2), the two afocal telescopes and deformable mirror to the lenslet and CCD camera is shown. It also shows the treatment beam traversing the reverse path to the eye. This arm is diffraction-limited with a point spread function Strehl ratio of 0.99. Therefore we can expect our spot patterns to be representative of the rat eye and not from aberrations of the HS optical path.

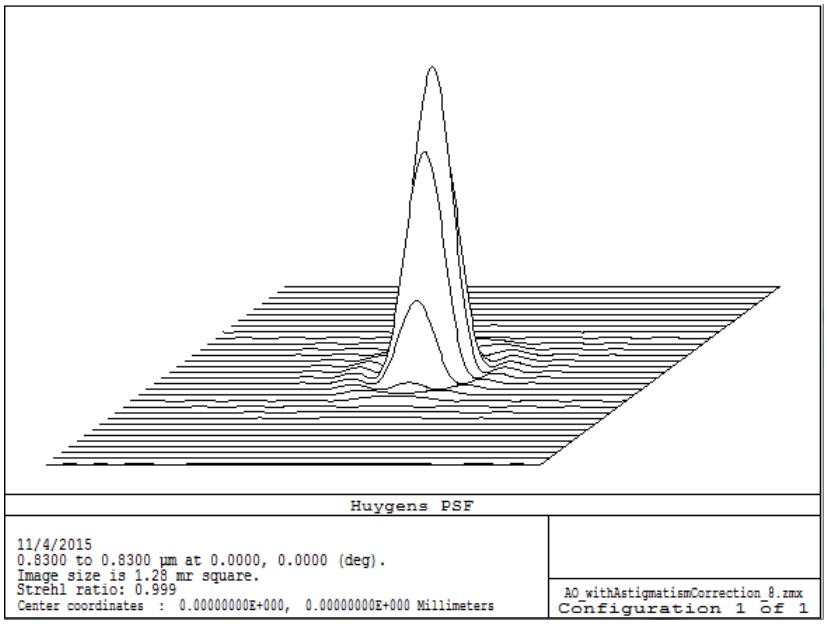

Figure 2.8: Verifying the HS arm and treatment beam from the eye to the CCD camera are diffraction-limited. With the astigmatism correction of the afocal telescopes the point spread function has a Strehl ratio of 0.99 which corresponds to a diffraction-limited system.

2.10 Conclusions

The goal was to model and construct an adaptive optics scanning laser ophthalmoscope to provide retinal images, wavefront measurement and correction and light delivery to the rat retina for two photon excitation. The main goal was to integrate the Xinetics 47mm apeture deformable mirror and construct a non-scanning wavefront sensor arm into the Waterloo confocal scanning laser ophthalmoscope. Using Zemax we were able to minimize the astigmatism introduced by two off-axis telescopes used to integrate the Xinetics deformable mirror. The astigmatism was first minimized by reducing the reflection angle of the spherical mirrors then subsequent correction using a cylindrical correction in a paraxial XY surface. In the actual system the correction was made by using two cylindrical lenses. After minimization of the astigmatism we verified that the HS optical path was

diffraction-limited, confirming that the primary contribution to the measured aberrations is the aberration of the eye with negligible contribution from the system aberration. Finally we checked the beam wander at the pupil of the eye in the scanning arm of the imaging optics, and determined that the deviation lay within the Airy disk of the stationary beam. This implies that the beam wander at the pupil of the eye is insignificant. According to this analysis, two photon excitation in the rat eye will be limited by our ability to correct the wavefront aberration of rat eye. It is expected that the limiting factors will be the correction of the second order aberrations, defocus and astigmatism, and the small stroke of our deformable mirror.

Chapter 3

Imaging and wavefront sensing of the rat eye

In this chapter an experimental situation analogous to those needed for two photon excitation (TPE) of the photosensitizer drug is shown. For the success of two-photon excitation in the rat eye, we aimed to minimize the lower order aberrations (defocus and astigmatism) using custom rigid contact lenses and spectacle lenses before adaptive optics correction (see chapter 4). After identifying a suitable vessel for closure, we need Hartmann-Shack (HS) spots sharp enough for wavefront sensing to correct the higher order aberrations (HOA) using an adaptive optics mirror, and remain centrally located for 7 minutes (Khurana, 2010).

In this experiment we will be focussing on achieving retinal images of the rat retina, identifying blood vessels that are a suitable size for blood vessel closure, observing sharp H-S spot patterns by using a contact lenses and static chromatic aberration correction in the HS and enabling the adaptive optics (AO) to correct the wavefront aberrations of the rat eye.

3.1 Methods

100 day old Long Evans rats were imaged using the adaptive optics scanning laser ophthalmoscope (AOSLO) with a 5 degree field of view. The rats were housed in standard rat cages under a 12 hour light to dark cycle. All animals were handled and experimental protocols according to the University of Waterloo Animal Ethics Committee as well as the Animal Utilization Project Protocol (AUPP). Rats were anaesthetized using isofluorane in an incubation chamber then subsequently held in a custom rat holder with a nose cone to maintain a surgical level of anesthesia. The pupil was dilated with 0.5% Mydryacyl. Retinoscopy was performed approximately 5 to 10 minutes after dilation to determine mean ocular refraction. A +5 to +17D rigid contact lens was applied to the cornea to maintain corneal hydration and correct the defocus measured via the retinoscopy during imaging.

To obtain retinal images and sharp HS spots simultaneously, we first imaged the retina with the contact lens in place to determine the location of the image plane relative to the surface of the retina. Due to the unexpected effect of the rigid contact lenses on defocus described in chapter 4, we used supplemental spectacle lenses to optically slice through the retina until we obtained suitable image quality of the retinal surface and vasculature. To improve spot quality as well as correct the chromatic aberration of the eye another spectacle lens was added in the HS arm until the HS spots were the sharpest.

3.2 Results

3.2.1 Initial attempt at imaging and wavefront sensing of the rat eye

In one rat, utilizing a +10D contact lens and +7D spectacle lens, with a 15mm vertex distance combination (+17.8D nominal correction in the CSLO arm, see chapter 4) we were able to obtain images of a blood vessel at the anterior surface of the retina, blood flow and feeder vessels that would be suitable for closure by TPE (shown in figure 3.1, left). Two vessels were identified which had vessel cross section diameters of A) 8.7 ±0.7um and B) 51.7±0.7um both suitable for blood vessel occlusion. Using the rat holder and the handler to position the eye in the system, we were able to remain in this location for approximately 30 seconds. However we were not able to keep a vessel centrally located in the SLO image without movement for two reasons. The rat holder did not allow for precise control of the head of the rat, to position the pupil in alignment with the exit pupil of the system. The rat handler had to manipulate the head with small movements to obtain retinal images. Additionally, we observed motion of the eye due to respiration of the rat and large eye roll.

A chromatic aberration correction of +3D relative to imaging arm, produced the sharpest spots possible in the HS arm. The HS pattern recorded with this correction corresponded to -2.5D of defocus and -0.5D of astigmatism refractive error for the second order aberrations. The spherical aberration was close to zero. In this first attempt to image the rat eye, we observed noise (figure 3.1, B) in our HS spots which caused instability in the adaptive optics mirror correction, therefore images with the wavefront corrected were

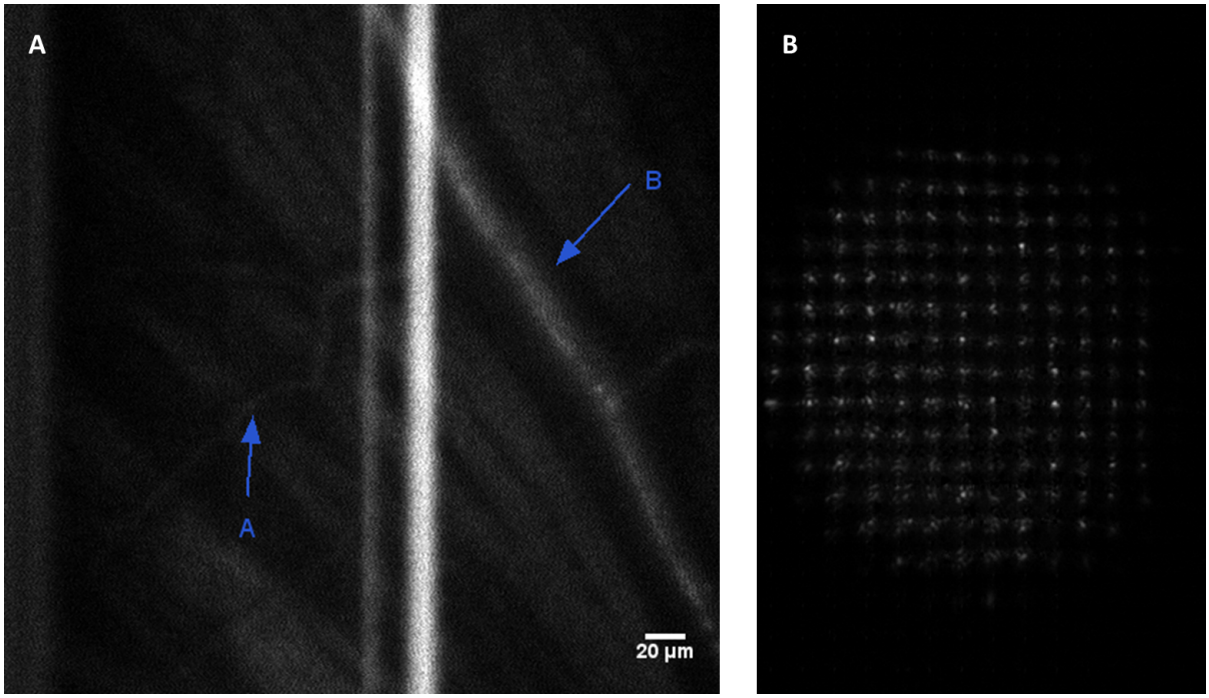

Figure 3.1: A, retinal image of rat with a +10D contact lens and +7D spectacle lens in a 5 deg field of view. Two blood vessels are shown with cross section diameters of A) 8.7 ±0.7um and B) 51.7±0.7um both suitable for blood vessel occlusion via two-photon excitation. B, the HS pattern recorded. The spots contained noise and caused deformable mirror instability and so we did not record images after wavefront correction.

not recorded.

3.2.2 Demonstration of wavefront correction of the rat eye

For a subsequent rat, (15D refractive error) with the adaptive optics mirror we were able to correct the wavefront aberrations of the rat eye as shown in figure 3.2, which showed the second order aberrations as a function of time. At frame number 50 the deformable mirror was activated, there is a sudden drop in the second order aberrations, from -2.5D of defocus and -1.5D of astigmatism initially to -1.5D of defocus and -0.5D of astigmatism refractive error after correction.

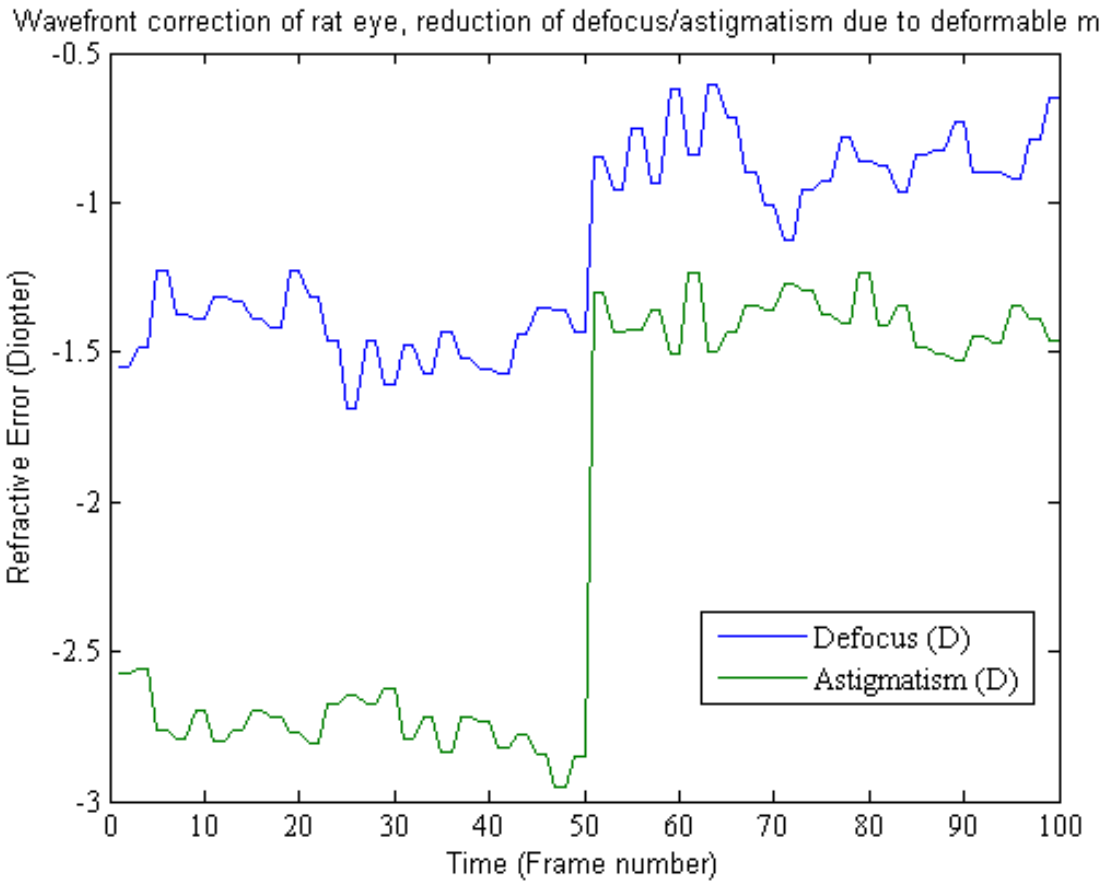

Figure 3.2: The x-axis is the time (frame number), and the y-axis is the RMS wavefront error in diopters. The HS recorded the defocus and astigmatism before and after AO correction (at frame 50).

We were able to minimize the noise previously observed in the HS spot pattern in figure 3.1 (B) in the new HS spot pattern in figure 3.3, allowing for stable wavefront sensing and correction. For this rat with +15D of refractive error, measured by retinoscopy, we were able to obtain very sharp spots, shown in figure 3.3, across the entire pupil after correction of the refractive error (with a spectacle lens) and adaptive optics correction. Unfortunately we were not able to obtain CSLO images simultaneously as they were very dark.

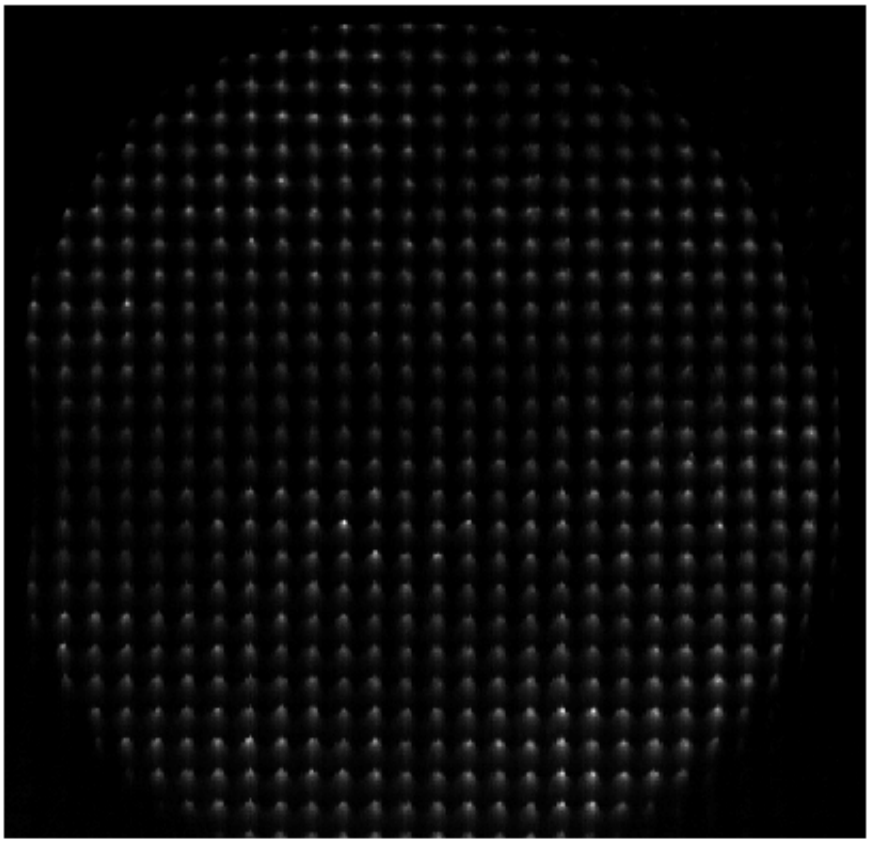

Figure 3.3: HS spots of rat corrected with +15D at the eye and adaptive optics correction. The spots are much sharper and less noisy compared to the HS spots in figure 3.1 (B).

Although the higher order aberrations were above the diffraction limit, they changed little when the AO was enabled, the spherical aberration however, changed sign from being approximately 0.01 waves before AO correction to -0.2 waves RMS afterwards, as shown in graph 3.4.

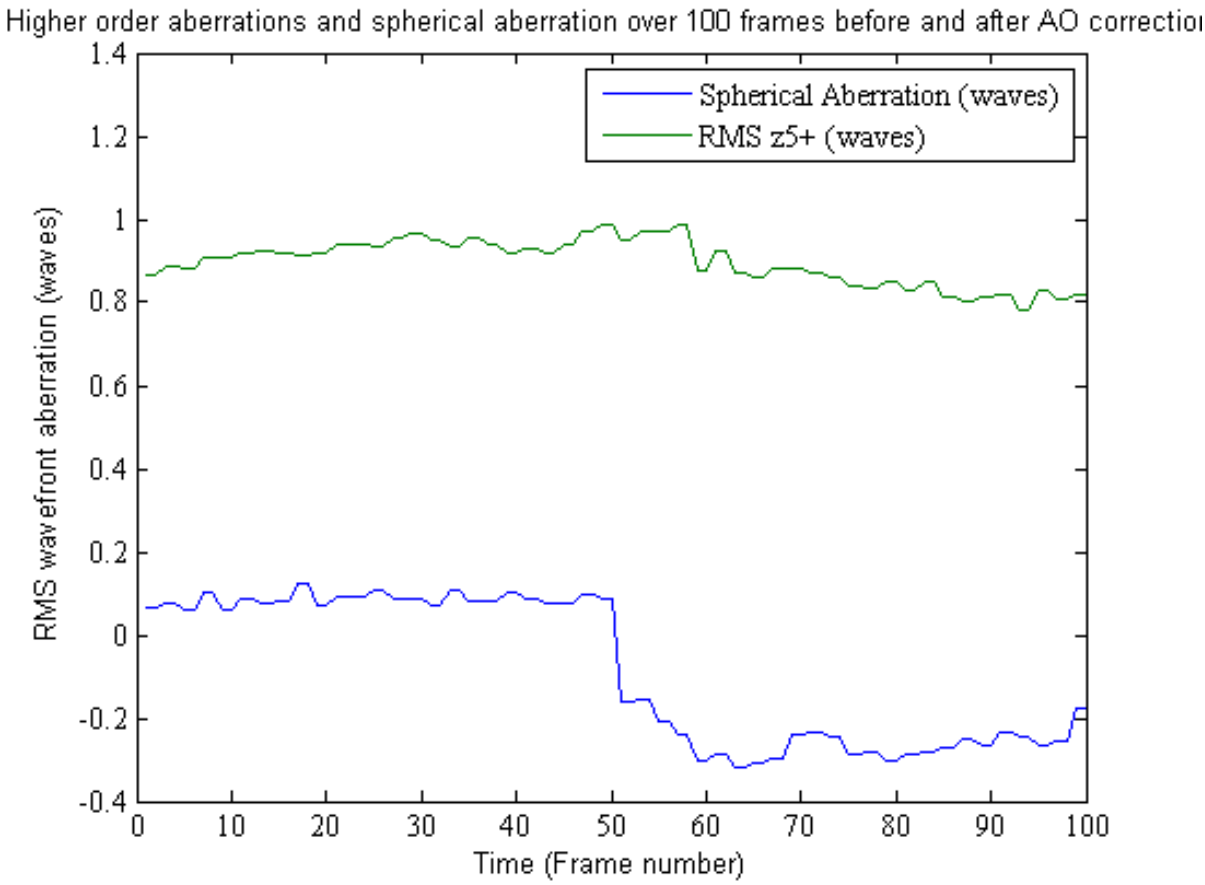

Figure 3.4: The x-axis is the time in frame number, and the y-axis is the number of waves of RMS aberrations (spherical aberration and RMS of the higher order aberrations, RMS of Zernike term 5 and higher). As the AO reduces the second order aberrations in figure 3.2, the higher order aberrations remain relatively unchanged, but the spherical aberration switches sign to -0.2 waves.

3.2.3 Eye movement

During our imaging sessions with the rat we observed two types of eye movement. The normal saccadic motion of the eye appeared to be minimized with the anaesthetic. We observed motion in the images because of respiration and large eye roll. The respiratory motion caused the retinal images to oscillate as shown in figure 3.5 which shows the maximum amplitude of oscillation. The eye movement was a lateral shift caused by the animal's

chest sitting flat in the rat holder. While the animal was breathing the entire body and head shifted. The large blood vessel is observed to be completely displaced by the diameter of the blood vessel.

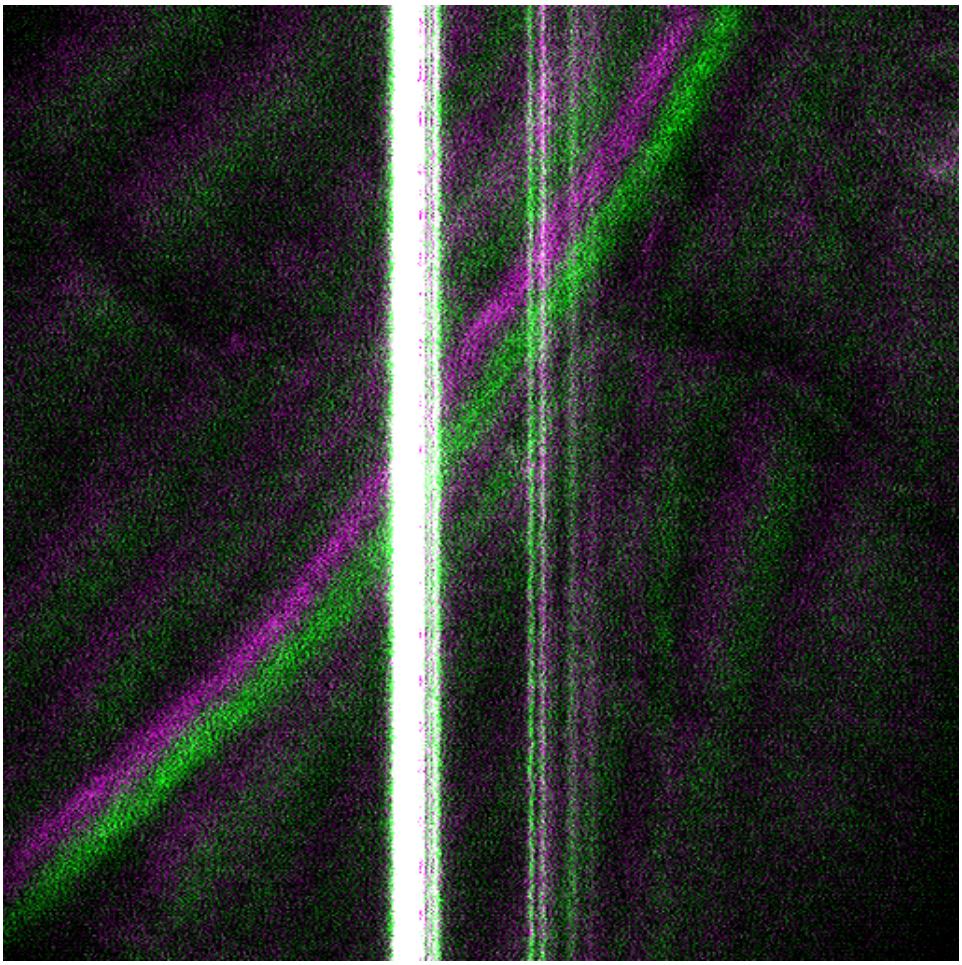

Figure 3.5: Overlay images of a rat retina at two different time points with vessel edges labelled in green at the first time point and purple at the second. The image shows an offset due to the animal breathing. The movement is significant enough that the large blood vessel appears to be doubled. The images were chosen at the largest amplitude of respiratory motion. The saturated vertical lines are a back reflection due to the x-axis scan

The second type of eye movement appeared to be large eye roll. Not shown here, but we observed the rat eye to drift a significant amount that the entire rat needed to be repositioned to image the same location on the retina.

3.3 Discussion

To emulate a two-photon excitation experiment we needed to image the retinal surface vasculature, identify a blood vessel and remain centrally located on the vessel for 7 minutes (Khurana, 2010). In their 2008 paper, Khurana and coauthers closed vessels with a 40±0.5um diamter in a window chamber mouse model (Mamta Khurana and Wilson, 2012) and we measured vessel cross section diameter, of similar size, approximately 9 and 50 microns in the rat eye. Additionally, we needed to ensure the HS beacon and treatment beam were focussed at the anterior surface of the retina after measuring and correcting the wavefront aberrations in order to locally activate the photosensitive drug.

Below I will discuss the challenges we encountered which need to be addressed before a TPE experiment can be carried out. Factors such as: noise in the HS spot patterns, the sensing plane and chromatic aberration of the rat eye, eye movement, and the large aberrations of the rat eye could constrain the success of a TPE experiment *in vivo* in the rat eye.

3.3.1 Noise in the Hartmann-Shack spot patterns

Imaging the first rat, we were able to identify blood vessels of suitable size for blood vessel occlusion however our HS spots were not sharp and appeared to have a poor signal-to-noise ratio. Between the first and second rat experiments we changed the magnification from the pupil to the HS lenslet and CCD camera from 1.11 to 2.22 times to increase the range of measurable aberrations in our system (in figure 3.1, B) and reduce the amount of blur due to the aberration change across the lenslet present in each HS spot. Minimizing the defocus

also helped to reduce the noise as the spots became sharper. Increasing the integration time of the CCD to average the light intensity and improve the signal-to-noise ratio of the camera also helped to improve the spot quality (figure 3.3 compared to figure 3.1B).

3.3.2 Determining the sensing plane of the Hartmann-Shack wavefront sensor

There are several factors which affect the ability to obtain diffraction limited images of the rat retina. The rat eye suffers from significant amount negative spherical aberration as the pupil size of the rat increases (M.C.W. Campbell, 1981) that degrades image quality. From the literature, the brightest reflex for infrared light is expected to be the photoreceptor layer of the retina (Ying Geng and Porter, 2009). There is a 130um focal shift between the retinal surface and the photoreceptor layer corresponding to an 8.9D shift (M.C.W. Campbell, 1981) and there is a 3.5D shift between wavelengths 633nm to 830nm (Hao Li, 2015) of chromatic aberration. Totalling 12.5D of correction required to move the focus of infrared light to the top of the retina under the assumption the bright reflex comes from the photoreceptor layer. It was found that using a +3D chromatic aberration correction to obtain the sharpest spots, the HS recorded -2.5D defocus which in the model of Campbell and Hughes corresponds to a 35.8um in thickness in the retina which is similar to the diameter of a blood vessel. This suggests the HS beacon was coming from the top of a vessel (while the surface of the retina was relatively sharp in the imaging channel in figure 3.1 A) or close to the retinal surface, and not the photoreceptor layers as suggested by Geng (Ying Geng and Porter, 2009). A reflection from the photoreceptor layer should have shown an 8.9D shift with respect to the retinal surface, before chromatic aberration

correction (Campbell, 1982). From the HS measurement, we can postulate that the HS beacon was reflected close to the surface of the retina which would imply that the treatment beam, which tracks the optical path of the HS, would be focussed close to the surface of the retina.

3.3.3 Wavefront correction of the Long-Evans rats

The significant amount of defocus and astigmatism limits the capability of the adaptive optics to correct the rat eye because of the small stroke Xinetics deformable mirror. The mirror has 4um (±2um) of stroke which corresponds to $z_2^0 = 1.15$um of defocus or 2.6D for a 3.5mm pupil. Therefore minimizing the low order aberrations was very important to see a reduction of the higher order aberrations. From figure 3.2 we see the AO mirror stroke being dominated by the second order aberrations which, after correction were reduced. However the HOA remained relatively unchanged as shown in figure 3.4.

The spherical aberration measured in rat 2, before and after correction changed from small negative value to a positive value as shown in figure 3.4. It was postulated that the contact lens may have had an affect on spherical aberration as the value was much lower than expected relative to the schematic eye model (M.C.W. Campbell, 1981). The presence of higher order aberrations, other than spherical aberration would be expected if the rat eye does not have the perfect axial symmetry assumed in the model or if the eye's pupil were not centered on the HS lenslet. If the eye was tilted so that aberrations were measured away from the optical axis, asymmetric aberrations would add to the axial spherical aberration. The 0.8 waves (figure 3.4) total higher order RMS aberration measured in the eye is slightly

smaller than the HOA (0.93 waves) of spherical aberration in the symmetrical eye model. This suggests that asymmetries in the real situation have converted symmetric spherical aberration to asymmetric HOA.

The eye movement observed in this experiment would affect the localization of the light dosage when using a photosensitive drug. The eye movement due to the animal's breathing may be corrected with a pupil tracking device or possibly reduced by use of head stabilization in the animal holder. Large eye roll makes the continual targeting over a period of several minutes of a suitable sized feeder vessel more difficult. The rat eye needs to be stable for wavefront sensing as well as blood vessel occlusion. A possible reason for the large movements could be our choice of anaesthetic. 1% isoflurane was shown to have the largest degree of eye movement(Govind Nair and Duong, 2011) relative to ketamine/xylazine and propofol. The choice of isolurane over ketamine/xylazine from past experiments was made due to the control over dosage levels, animal recovery time as well as a lower occurrence of cataract development. It may be worthwhile to try 1% isoflurane with a paralytic as it was shown to minimize most eye movements(Govind Nair and Duong, 2011) compared to the addition of a paralytic to the other drugs mentioned above.

3.4 Conclusions

We were able to successfully image the rat eye and measure the wavefront aberration in the AOSLO. From measurements of the wavefront aberrations and the SLO images we were able to determine that with a chromatic aberration correction in place, when the imaging channel was focussed on the surface of the retina, the Hartmann-Shack wavefront beacon appears to be focussed just above the surface of the retina instead of deeper in the photoreceptor layer. Therefore the treatment beam for two-photon excitation would also be focussed close to the anterior blood vessel layer of the eye as the beam path is coincident with the HS optical path and the amount of chromatic aberration between the HS and treatment beams is small. Using the Xinetics deformable mirror we were able to show correction of the low order aberrations of the rat eye. Alternatively, a larger stroke AO mirror could be used to correct both lower and higher order aberrations. Finally, eye movement due to respiratory motion may affect the efficiency of the treatment and head stabilization, pupil tracking and/or the use of a paralytic with the anaesthetic may need to be explored. From these results, minimization of the second order aberrations with a contact and spectacle lens combination could be very important for two-photon excitation in the rat eye using this apparatus. Furthermore, the small amount of spherical aberration recorded and the large refraction correction observed with the initial contact lens in place, prompted investigation of the effect of the contact lens on the schematic eye model in the following chapter.

Chapter 4

The Effect of Rigid Contact Lens Parameters on Wavefront Aberration of the Rat Eye

The aberrations of the rat eye have a significant impact on the success of two-photon excitation (TPE) as a treatment of age-related macular degeneration (AMD). The rat eye has a significant amount of defocus and spherical aberration, due to the Gradient Index (GRIN) lens having over-corrected (negative) spherical aberration (Campbell, 1982). These ocular aberrations degrade the quality of retinal images and as a result adaptive optics (AO) is required to correct aberration. The aberrations affect retinal image quality and light entering the eye, spreading the intensity over a larger blur spot reducing the probability of TPE (Bird, 2006). In his thesis, Bird utilized Campbell's elliptical and spherical shell model eye to determine the affect of the ocular aberrations on image quality and TPE. Bird determined that the significant amount of defocus and spherical aberration would limit the probability of TPE and therefore AO would be required to carry out TPE of a photosensitive drug. While imaging an anesthetized rat, the eye suffers from tear film break up and cataract formation. Typically, artificial tears are applied every few minutes to maintain corneal hydration, however this complicates acquiring retinal images over long

durations. In the past, researchers have used a variety of methods to maintain corneal hydration and statically correct the low (second) order aberrations with spectacle lenses, fundus lenses and contact lenses which will be discussed, in addition to AO.

Imaging rat eyes with a spectacle lens requires artificial tears to be applied every few minutes to provide corneal clarity, hydration and prevent cataract formation. The downside of using a spectacle lens in front of the rat eye is the need to minimize the vertex distance between the lens and the eye as well as tilting the lens to remove any back reflections which also introduces astigmatism.

A refractive power cancelling fundus lens has been used to remove optical aberrations for a mouse model and could potentially be used for rats. The fundus lens works by cancelling the refraction of the cornea, significantly reducing the power of the eye. The combination of an objective lens in front of the eye and the fundus lens acts as an aberration free combination to help focus light on the retina, increasing the focal length of the eye. However, the cornea and the crystalline lens spherical aberration in the rat are of opposite sign (Campbell, 1982), so the total aberrations could increase when the cornea is neutralized. When using a fundus lens, one encounters a number of trade-offs between imaging capability, TPE, and AO correction. The fundus lens allows for easy alignment with the exit pupil of the system, removes corneal back reflections and keeps the eye hydrated (Y. Jian, 2013). Increasing the f-number of the rat eye would allow optical slicing through the retina with a smaller stroke deformable mirror but reduces the lateral resolution, as well as lowering the probability of TPE.

Rigid contact lenses with an eye lubricant have been used to maintain cornea hydration

(Ichiro Kawaguchi, 2006, X Liu and Jiao, 2013), as well as to correct the lower order aberrations of the rat eye (Ying Geng and Porter, 2009). Contact lenses can be designed with different base curvatures and powers to fit the rat eye. Powerless contact lenses have been shown to improve the image quality of optical coherence tomography (OCT) images of the rat eye by maintaining corneal hydration and giving partial ocular aberration correction (X Liu and Jiao, 2013). The drawback to contact lenses is that a mismatch between base and corneal curvatures can cause unpredictable correction. In the literature, a slit lamp and retinoscopy have been used to measure the corneal curvature and refractive power to determine the contact lens shape required for imaging the rat eye (Ying Geng and Porter, 2009). Here, custom shaped rigid contact lenses were used when imaging the rat eye because they have been shown to improve image quality and Hartmann-Shack spot patterns, and maintain corneal hydration over long durations. The contact lens also preserves the low f-number of the rat eye which correlates with the probability of TPE.

The main goal of this chapter is to demonstrate the effect of the base curvature of the contact lens on image quality, Hartmann-Shack (HS) spots and TPE. The power of the contact lens was determined through retinoscopy after pupil dilation, and the base curvatures were taken from Campbell's eye model (Campbell, 1982). After the contact lens was applied, the HS spot patterns showed large blurry spots, and we had to add an additional spectacle lens in front of the rat eye to improve the spots and attain retinal images. The need for this overcorrection was unexpected and prompted an investigation into it's cause, which is the main focus of this chapter. The proposed experiment was to measure the wavefront aberrations of the rat eye with and without a contact lens and

compare them to Campbell's optical model with a contact lens and tear lens. The main result is that rigid contact lenses can be made to correct the lower order aberrations of the rat eye and can also improve image quality due to the correction of higher order aberrations.

4.1 Optical Model

In her 1982 paper, Campbell proposed two different rat eye models fit to experimental measurements for surface positions and surface curvatures(Campbell, 1982). The spherical shell model used a lens with spherical isoindicial surfaces and a spherical cornea, and was created for 140 day old rats. The elliptical shell model (ESH) used a corneal surface with a conic constant of $k = -0.238$, and ellipsoidal isoindicial lens surfaces, which created a thin shell at the lens surface for 115 day old rats as shown in table 4.1. Isoindicial surfaces, used to create the lens, are surfaces where the index of refraction is constant over their entire extent. Other surface curvatures, such as the retina surface and outer limiting membrane did not show any age dependence and were made the same between the two models. In this experiment, we were primarily imaging younger rats, around 100 days old, therefore the ESH model was chosen as the basis of comparison to experimental results.

The elliptical shell model (ESH) in figure 4.1 shows the components of the rat eye composed of a highly curved corneal surface, a gradient of refractive index (GRIN) lens, the retina, and outer limiting membrane. The refractive state (defocus error) of the rat eye depends on many optical parameters, such as pupil size and surface curvatures, variations in positions of the optics (Campbell, 1982), pigmented versus albino rats due to more light scattering through the iris, age and the use of anaesthetic (Tkatchenko and Tkatchenko,

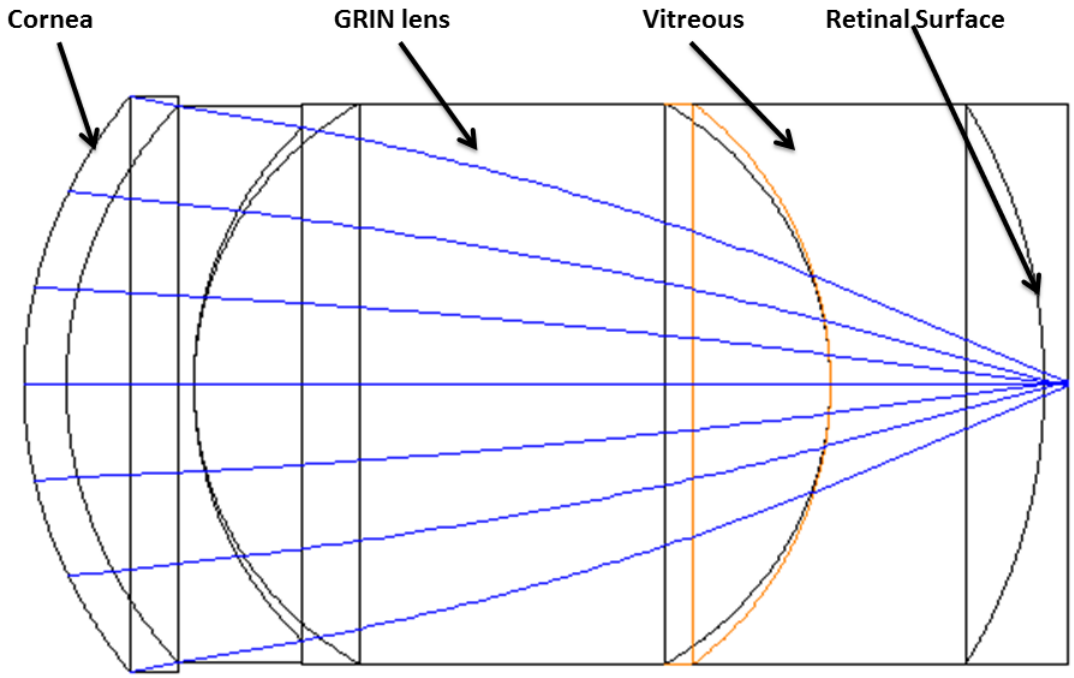

Figure 4.1: Schematic of the Campbell elliptical shell model. The figure was adapted from Bird.

2010), and as a result has been reported to range from 12D of myopia to 20D of hypermetropia (A. Chaudhuri, 1982). The refractive state of the ESH model is -2.5D with a range from -1.1D to 6.6D for a small pupil with respect to the photoreceptor layer due to a variation in the crystalline lens model. However the refractive state moves hypermetropic as the pupil dilates due to spherical aberration (M.C.W. Campbell, 1981) with respect to the photoreceptor layer of the eye. In the ESH model we used a wavelength of 550nm and the refractive error is +9.4D with respect to the surface of the retina for a 3.5mm entrance pupil.

Table 4.1: The positions, curvatures and conic constants of each surface in the rat eye relative to the anterior corneal surface(Campbell, 1982) of the Elliptical Shell Model (ESH). These values were used to model the aberrations of the rat eye for a 115 day old rat

Surface	Position (mm)	Radius of Curvature (mm)	Conic Constant (k)
Anterior cornea	0.000	2.680	-0.238
Posterior cornea	0.250	2.430	-0.238
Anterior lens	1.000	2.290	0.226
1st boundary of GRIN	1.000	2.006	0.074
2nd boundary of GRIN	4.736	-2.006	0.074
Posterior lens	4.736	-2.290	0.226
Retina surface	5.992	-3.457	0.403
Outer limiting membrane	6.132	-3.597	0.403

For TPE to be successful in the rat eye, it is necessary to have a lot of power in a tight volume, and to move the light towards the surface of the retina because the blood vessels of the rat are close to the retinal surface. As a next step, demonstration of the closure of a vessel on the anterior retinal surface is planned. Thus in this study, a focus close to the retinal surface was considered ideal. It was confirmed during our experiments using retinoscopic measurements that the Long Evans rats were hypermetropic as suggested by Campbell for another pigmented strain, Dark Agouti (DA) rats. The schematic eye model predicts that on-axis aberrations of the eye are made up of a significant amount of defocus and over-corrected spherical aberration.

4.2 Methods

4.2.1 Rats and preparation for in vivo imaging

For this experiment, Long Evans rats were imaged. All of the rats were approximately 100 days old at the time of imaging. The rats were housed in standard rat cages under a 12 hour light to dark cycle. All animals were handled according to the University of Waterloo

Animal Ethics Committee as well as the Animal Utilization Project Protocol (AUPP). Rats were anaesthetized using isofluorane in an incubation chamber then subsequently held in a custom rat holder with a nose cone. The pupil was dilated with 0.5% Mydryacyl. Retinoscopy was performed approximately 5 to 10 minutes after dilation to determine mean ocular refraction. A +5 to +17D rigid contact lens with a base curve of 3.1mm was applied to maintain corneal hydration during *in vivo* imaging and correct defocus measured via retinoscopy.

4.2.2 Hartmann-Shack measurements of the rat eye and extending the Campbell model with a contact lens

The aberrations, including defocus, of the rat eye were measured with a Hartmann-Shack (HS) aberrometer. To compare the effects of a spectacle lens, contact lens and the combination, spot patterns were recorded without correction, with a spectacle lens and a contact lens of the same power separately and with a contact-spectacle lens combination. Initially, contact lenses matched the refraction measured by retinoscopy. The spectacle lens was used to zero the residual defocus not corrected by the contact lens, as measured by the HS. The custom rigid contact lenses used were designed with an index of refraction $n = 1.442$, a base curvature of 3.1mm and 0.3mm center thickness (confirmed by the manufacturer for a 2mm entrance pupil), ranging in powers from +10D to +17D.

Using the manufacturers specifications above, the custom contact lenses were added to the ESH model created by Campbell and Hughes (M.C.W. Campbell, 1981) and initially modelled in Zemax by Bird (Bird, 2006). Zemax was used to determine the front surface curvature of the contact lenses, r_1, for powers of 10D, 12D, 15D, 17D and 20D, as they

were not specified by the manufacturer. To extend the modelling beyond our custom rigid lenses, the base curvature, r_2, was varied while keeping the contact lens power constant using the method above to determine the anterior surface of the contact lens. The base curvature was varied from steep to flat relative to the corneal radius of curvature and the spherical aberration and the power of the disk of least confusion were recorded. To measure the aberrations in the same plane for all configurations of the contact lens, a paraxial surface, acting as a spectacle lens, was used to focus the light to the surface of the retina. The power of the spectacle lens and Strehl ratio, a measure of image quality, were also recorded.

4.3 Results

4.4 Hartmann-Shack measurements of the rat eye with contact and spectacle lens correction

Figures 4.2 and 4.3 show the HS patterns of a rat eye, measured to have 12D of refractive error with retinoscopy, with a spectacle lens and contact lens correction respectively. During imaging sessions with the AOCSLO we found that the contact lens was not correcting the rat eye as expected compared to using a spectacle lens with similar power. The HS measured zero defocus with a 12D spectacle lens with a vertex distance of 20mm making the spectacle lens effectively a 15.8D lens at the pupil. The HS spot pattern is shown in figure 4.2 with a spectacle lens correction, with some residual astigmatism, negative spherical aberration and other higher order aberrations causing the blurred spots. If we consider the effective power of the spectacle lens as the power to correct the eye (15.8D),

there is a residual 6D of defocus needed with the nominally 12D contact lens as shown in figure 4.3, indicating that on the eye, it provided less than its nominal power. The HS also measured -0.6 waves of spherical aberration and 1.2 waves of 3rd and 4th order RMS HOA which are lower than the model's prediction. It was suspected that the fit of the contact lens on the corneal surface may have a significant effect on the refractive error correction and the spherical aberration measured. However, differences between HS measurements and retinoscopic measurements may also contribute to variation observed and so will be discussed below.

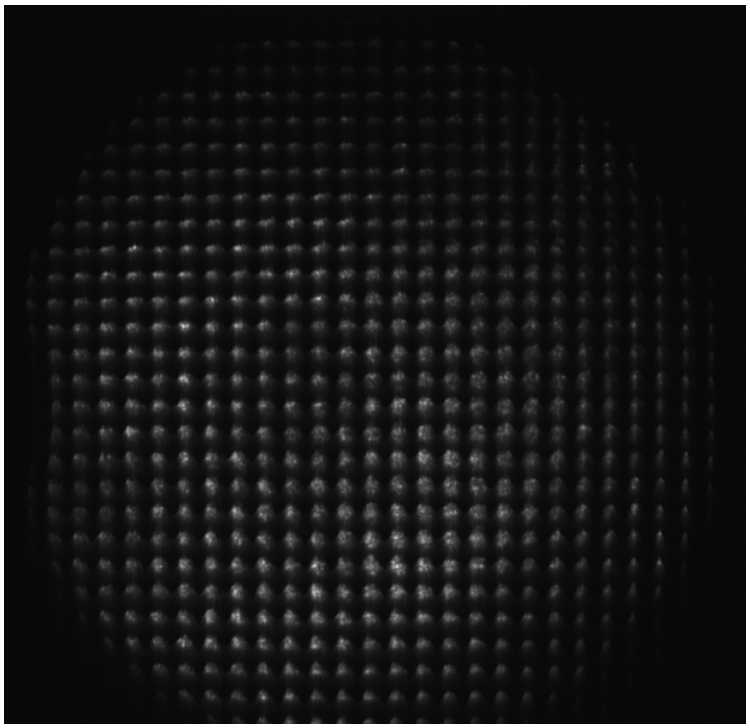

Figure 4.2: A HS pattern of a rat eye with a +12D spectacle lens with a vertex distance of 20mm making it a 15.8D lens at the pupil of the rat eye which zeroed the HS defocus. The somewhat blurred spots could be due to residual astigmatism, spherical aberration (-0.5 waves) and other higher order aberrations (3rd and 4th order RMS 1.6 waves).

A second imaging session was conducted with another rat with the intention to zero

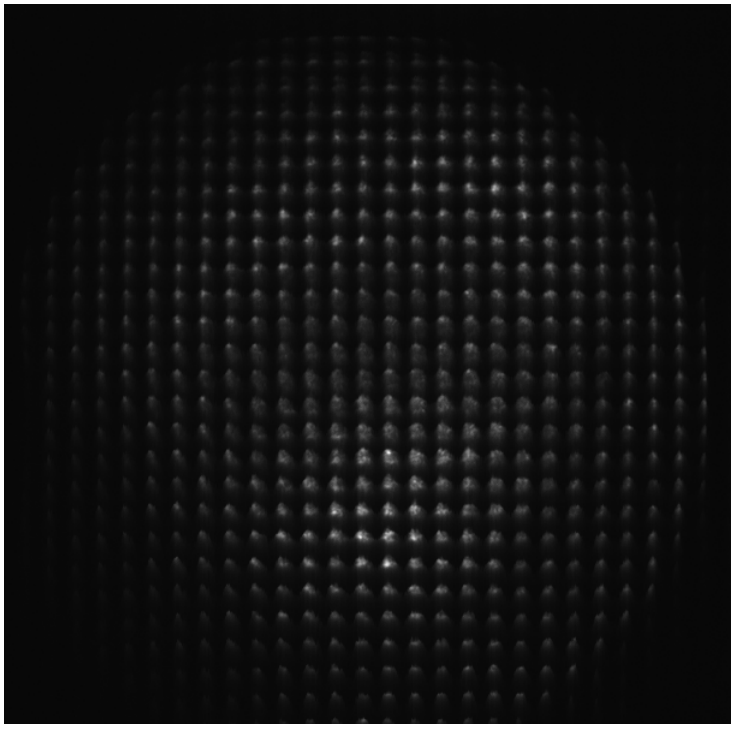

Figure 4.3: HS pattern of the rat eye in figure 4.2, with a +12D contact lens with a base curve of 3.1mm. The retinoscopy determined +12D was required for correction. The HS measured 6D of residual defocus and -0.6 waves of spherical aberration. The 1.2 waves of 3rd and 4th order RMS HOA with this contact lens on the eye is less than that of the eye with a spectacle correction (1.6 waves). The spot quality could be due to both the residual defocus and spherical aberration, any astigmatism and other higher order aberrations. Given that a spectacle correction of 15.8D corrected the eye, the 12D contact lens on the eye was giving less than its nominal power.

the defocus using a contact lens and spectacle lens combination. The retinoscopy showed approximately 12D refractive error and a 12D contact lens was used. In this case however a -1D spectacle lens with a vertex distance of 24mm (effectively -1.025D) was required to zero the defocus with -0.42 waves of spherical aberration measured, the resulting HS pattern is shown in 4.4. In contrast to the results from the first rat, in this case the contact lens was found to over-correct the refractive error.

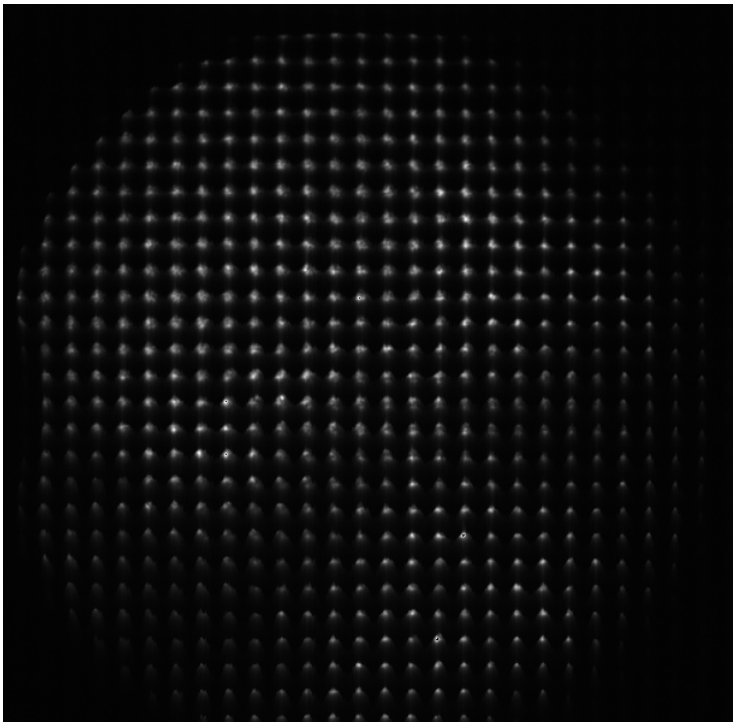

Figure 4.4: An HS pattern of a second rat eye with a +12D contact lens and a -1D spectacle lens. The defocus is zeroed with a residual -0.4 waves of spherical aberration and 0.7 waves of 3rd and 4th order RMS HOA is less than that predicted for the eye alone (-0.9 waves) and less than that measured in rat 1 with a spectacle correction. The spot quality has improved with respect to figures 4.3 and 4.2. In this case the spectacle correction required to zero the defocus was opposite in sign to the previous rat with a similar refractive error and the same contact lens correction.

The spot quality of the HS pattern in 4.4 was considerably sharper compared to both figures 4.2 and 4.3 and there were fewer 3rd and 4th order higher order aberrations present with a contact lens correction than with the spectacle lens correction. The amount of higher order aberration with the same contact lens correction differs between rats.

4.4.1 Optical Modelling: Varying the base curvature of the contact lenses with constant paraxial power on the elliptical shell model of the rat eye

Investigating the experimental observations from the previous section, the power and spherical aberration of custom rigid contact lenses are tabulated in table 4.2 for the entrance pupil sizes 2mm and 3.5mm. The undercorrected (positive) spherical aberration increases and gives an increased power relative to the nominal power of the contact lens for the larger 3.5mm entrance pupil. The difference in power can be attributed to the amount of positive (undercorrected) spherical aberration that is introduced with the pupil size change. The spherical aberration increases as the front surface of the contact lens becomes steeper for the 10D to 17D lenses with a constant base curvature. The spherical aberration changes with a different base curvature but the front surface was chosen to maintain a constant nominal power of the contact lens as shown in table 4.2, for the two 15.5D lenses. However, because of the changes in spherical aberration and in the tear film, the powers of these two contact lenses on the eye differ.

Table 4.2: A table comparing contact lens power for 2mm and 3.5mm entrance pupils due to the spherical aberration at the larger pupil size causing a change in power (last column). The first four lenses are described by their nominal power and the last 2 lenses vary in base curve but maintain 15.5D nominal power illustrating two lenses with similar power at small pupil sizes can differ in power at large pupil sizes as a consequence of their respective curvatures.

Contact lens	Front, r_1(mm)	Base, r_2(mm)	Power(D) @ 2mm	Power(D) @ 3.5mm	ΔPower (D)
10D	3.00	3.10	9.33	12.840	3.51
12D	2.97	3.10	11.21	15.38	4.17
15D	2.91	3.10	15.02	19.20	4.19
17D	2.87	3.10	18.02	23.04	5.02
15.5D	2.57	2.68	15.52	21.47	5.96
15.5D	2.90	2.75	15.43	20.09	4.65

To determine how the base curvature, r_2, of the rigid contact lens affected the correction of the rat eye, contact lenses with varying base curvatures were applied to the elliptical shell model using Zemax, for a 115 day old rat. The thickness of the tear lens, the water layer between the contact lens and cornea, was kept as small as possible for all shapes of lenses. For steeper lenses, $r_2 < r_{cornea}$, the tear lens thickness was set to zero at the edges of the contact lens so the tear fills the space between the cornea and contact lens at the center of the eye (figure 4.7) or for flatter lenses, $r_2 > r_{cornea}$, the thickness of the tear film was set to zero at the center of the lens and the tear filled the space at the edges of the cornea (figure 4.6). This constrained all lenses to sit on the surface of the cornea similar to the way they are known to sit on the eye. A spectacle lens was adjusted to keep the image focussed on the surface of the retina as shown in figure 4.5.

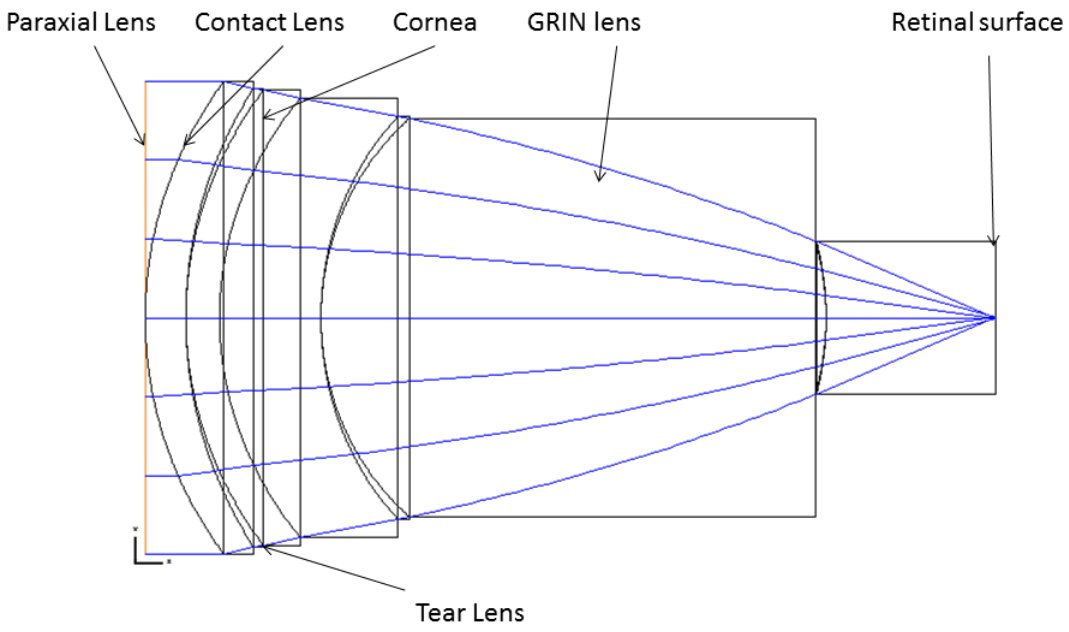

Figure 4.5: Schematic of the rat eye model with a contact lens and a "paraxial" spectacle lens placed at the front of the rat eye. The space between the contact lens and the cornea is filled with an index of refraction of $n_{water} = 1.33$ to act as a tear film. A spectacle lens is used to compensate for any defocus shift that the contact lens does not correct when on the model eye.

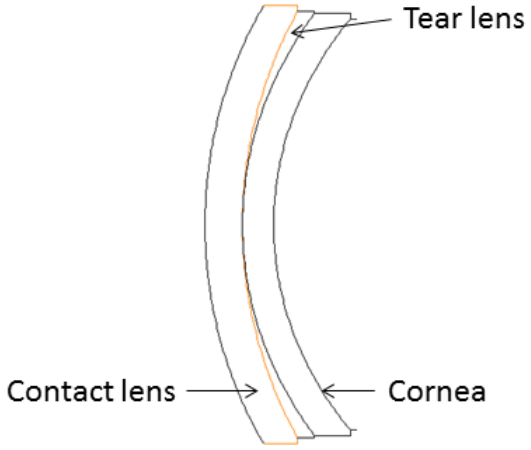

Figure 4.6: The base curve of the contact lens (orange) is flatter than the cornea and the tear lens fills the edges. There is no separation between the contact and cornea at the center of the cornea

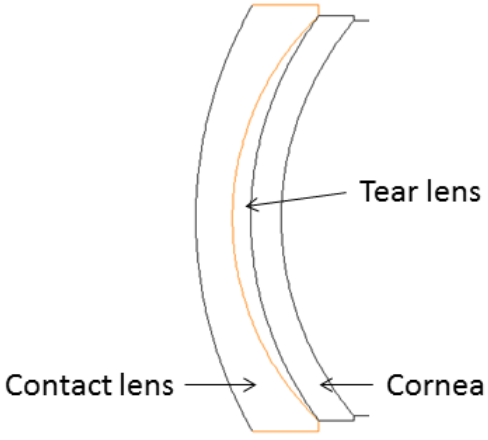

Figure 4.7: The base curve of the contact lens (orange) is steeper than the cornea and the tear lens fills the center. There is no separation between the contact and cornea at the edges of the cornea.

Table 4.3: Resulting power of the contact and tear lens combination with the anterior radius of curvature of the tear lens of 3.1mm, matching the back surface curvature of the contact lens, and the posterior radius of curvature of the tear lens matching the corneal radius of curvature, $r_{cornea} = 2.68mm$. The contact lens front surface curvature is varied to give the desired nominal power. The tear lens significantly affects the overall power of the contact lens and tear lens combination, in some cases negating the contact lens power. The spherical aberration remains positive and increases with the power of the lens.

Nominal Contact Lens Power (D)	Lens and Tear Lens Power (D)	Spherical aberration (waves)
10D	-5.047	0.425
12D	-3.183	0.545
15D	3.966	0.727
17D	6.890	0.913
15.5D	27.568	2.073
15.5D	13.410	1.280

The tear lens was created by using the base curve of the contact lens and the front corneal surface as the front and back surfaces of the tear lens respectively. Due to the difference in radius of curvature of the contact lens and cornea, the tear lens can form a lens when $r_2 < r_{cornea}$ and has a negative focal length or when $r_2 > r_{cornea}$ which has a positive focal length. It was found that when including the tear lens in the model with a contact lens with base radius of curvature of 3.1mm, the power of the contact and tear lens combination was significantly less than the nominal power of the contact lens. In table 4.3 the affect of the flat tear lens is shown to be very significant on the power of the contact lens. The powers of 10D and 12D lenses are completely negated by the tear lens, but the combination still had positive spherical aberration.

Spherical aberration is known to be dependent on paraxial lens power, so the front surface of the lens was varied to give a constant paraxial lens power for different base curvatures of the contact lens on the ESH model. Any change in spherical aberration of the lens with a base curve change would then change the nominal lens power for a 2mm

pupil. Varying the base curvature changes the shape of the tear lens and the combination results in a significant difference in power compared to the nominal power of the rigid contact lens (figure 4.8). The spectacle lens in front of the eye compensated for this residual defocus and moved the best focus to the top of the retina. In figure 4.8 the power of the spectacle lens required corresponding to each base curve is plotted for each contact lens power. The plot shows that as the base curvature increases from 2.5mm to 3.5mm there are differing contact lens power and base curvature combinations that do not require an additional spectacle lens to image the retinal surface. The contact lenses that do not need additional defocus have base curvatures: 2.85, 2.9, 2.97, 3.03 and 3.1mm for the 10, 12, 15, 17, 20D nominal lens powers respectively, all of which are flatter than the corneal radius of curvature $r_{cornea} = 2.68$mm and correct the rat's defocus for a 3.5mm pupil. In these cases the tear lens changes the power of the contact lens. From figure 4.8 a positive power spectacle lens is required while using flatter contact lenses to move the best focus to the retinal surface.

Clearly, the shape of the contact lens is important for defocus correction, image quality and practical use in an experiment. The larger the mismatch between the lens base curve and the corneal front surface ($r_{cornea} = 2.68mm$), the larger the positive (for flatter fits) or negative (for steeper fits) spectacle powers that need to be used to focus at the top of the retina. These powers of spectacle lenses are unrealistic to use in an experimental setting. The large curvature mismatch of the contact lenses with extreme base curves to the cornea ($r_{cornea} = 2.68mm$) could cause the lenses to fall off during an experiment. A plot of image quality (Strehl ratio) against the base curves of contact lenses of differing powers,

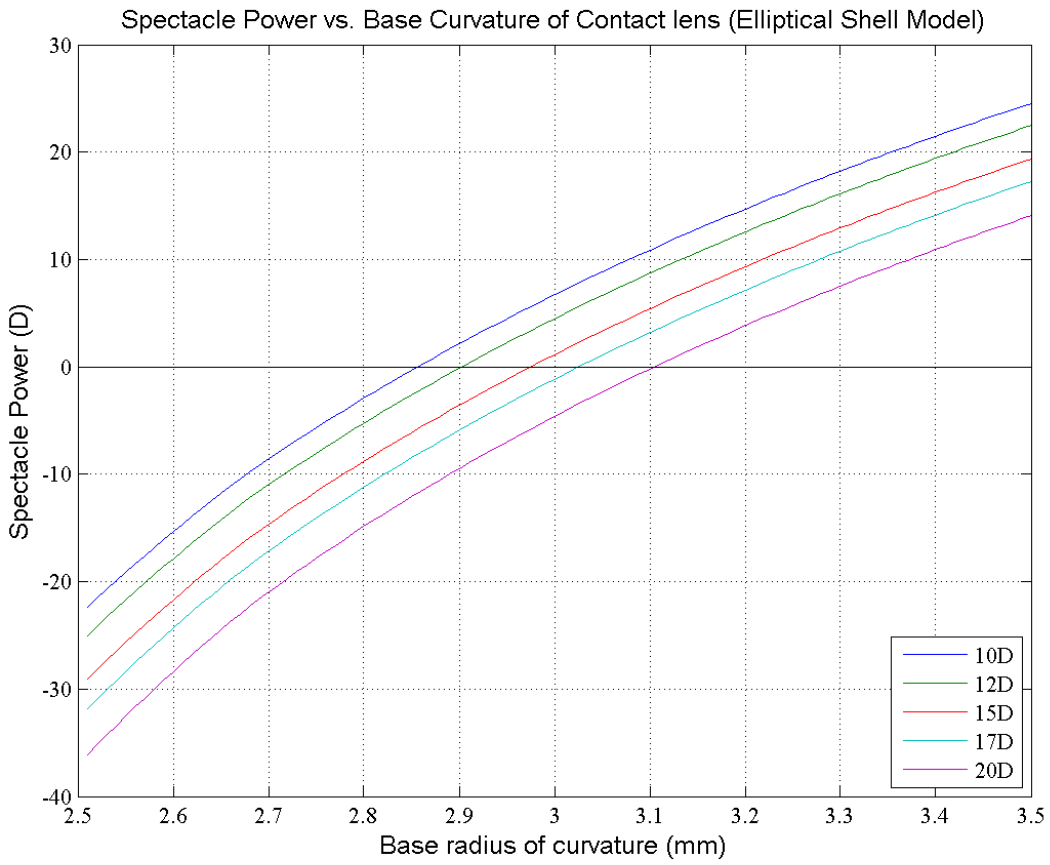

Figure 4.8: The x-axis is the base curvature of the contact lens, the y-axis is the corresponding spectacle lens in front of the eye to move the focus to the retinal surface. There exists a unique base curve for each power of lens that allows the contact lens to image the surface of the retina without additional spectacle correction, given as the intercept of the curve for each lens power with the horizontal line of zero lens power.

in figure 4.9 shows that for a small range of curves the Strehl ratio is high for each power of contact lens. In this case there was no contact lens that reaches the maximum Strehl ratio at a base curve which matches the corneal radius. The image peak in the Strehl ratio did not correspond with the base curvatures that required no correction with a spectacle lens (figure 4.8). As the nominal power of the contact lens decreases the maximum of the Strehl ratio moves towards flatter base curves (figure 4.9).

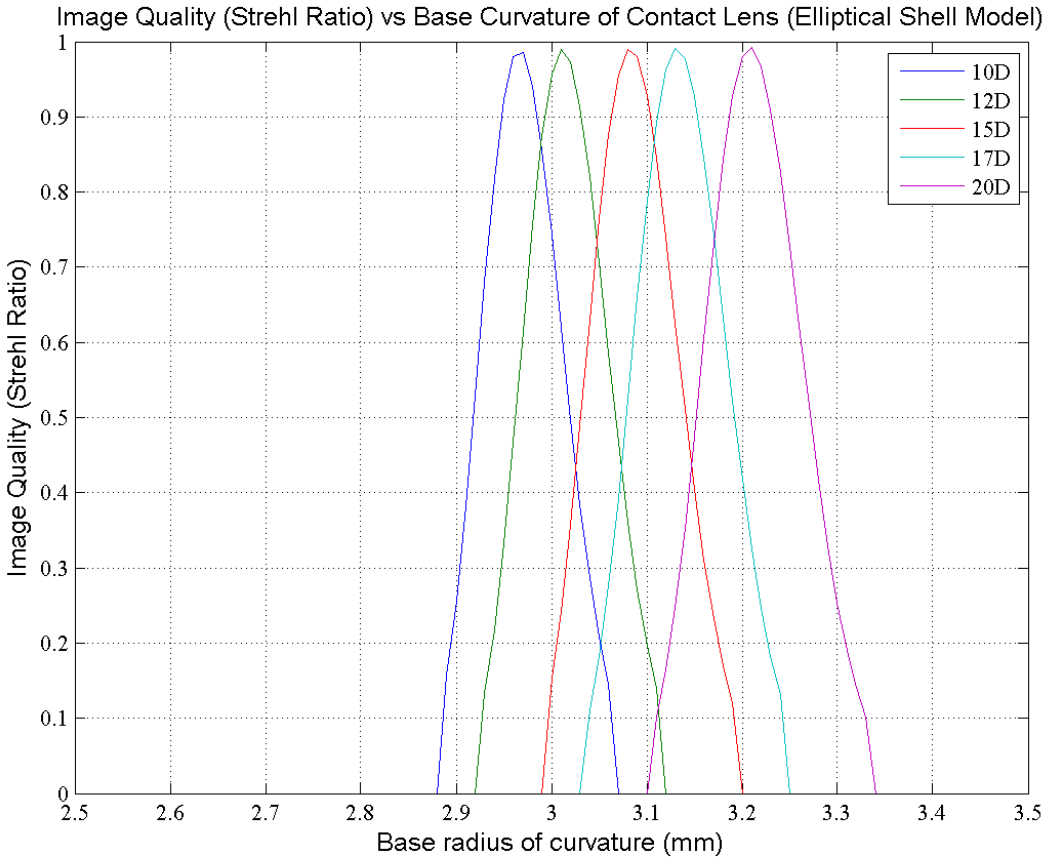

Figure 4.9: The x-axis is the base curvature of the contact lens, the y-axis is the Strehl ratio evaluated at the retina surface for the ESH model for the higher order aberrations only. The values are un-normalized and since we are only looking at the on-axis aberrations the image quality increases significantly when the spherical aberration of the rat eye is corrected by the contact lens on the eye. Residual defocus has been corrected with a spectacle lens. The corneal radius of curvature for the ESH is $r_{cornea} = 2.68$mm with a conic constant of $k = -0.238$ meaning flatter at the edges of the pupil.

The above results show that a change in shape of the tear lens causes a change in defocus and potentially spherical aberration. Spherical aberration is also known to vary with the change of base curvature or power of a contact lens. A plot of the spherical aberration against the base curvatures shows the more highly curved contact lenses have positive spherical aberration when combined with a tear lens and the eye, and as the contact lens

flattens the spherical aberration decreases and becomes negative as shown in figure 4.10.

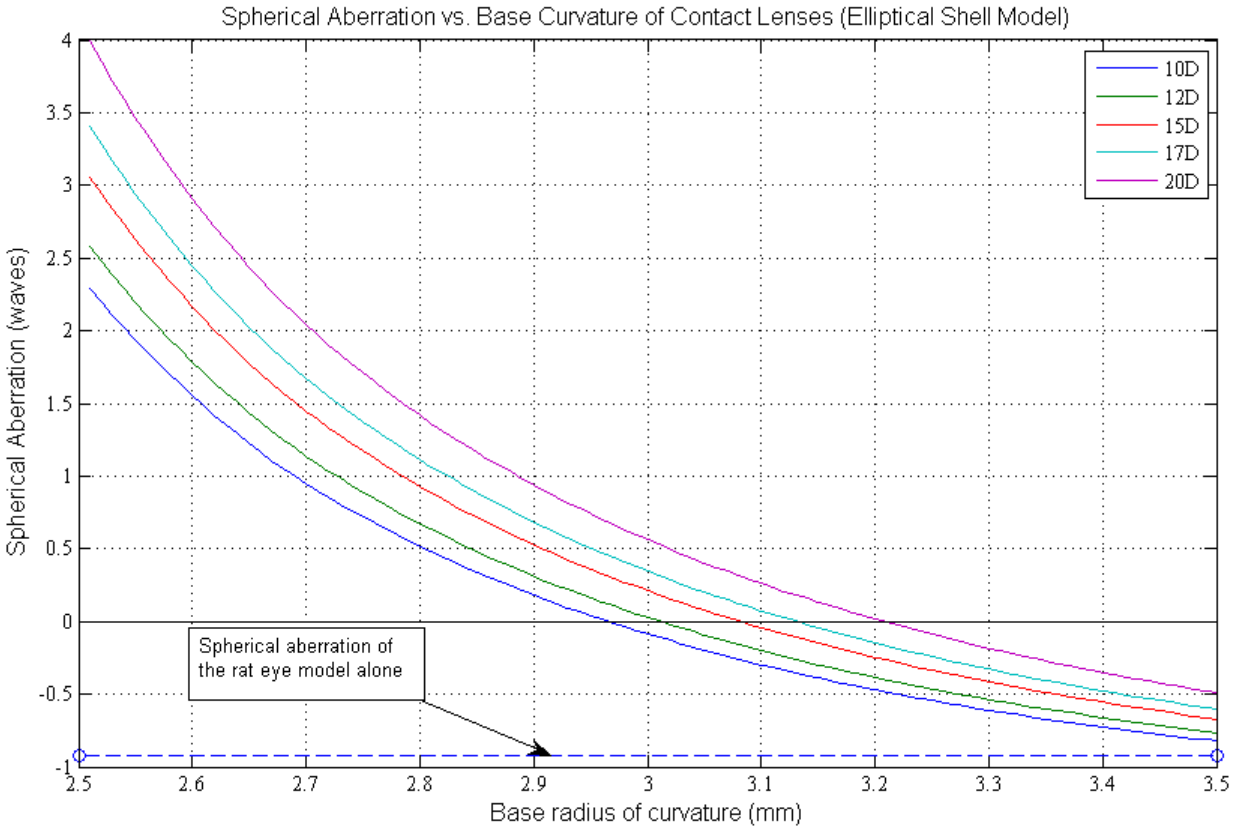

Figure 4.10: The x-axis is the base curvature of the contact lens, the y-axis is the spherical aberration of the contact lens on the eye in waves. Varying the base curve from steep to flat radius of curvature relative to the corneal radius of the rat eye changes the spherical aberration of the contact lens and tear film combination. The power of each lens was held constant across a 3.5mm pupil diameter and the spherical aberration of the contact lens plus tear lens plus rat eye decreases with a flatter base curve. The spherical aberration of the contact lens plus the eye model is always more positive than the spherical aberration of the rat eye alone.

The ESH model has negative spherical aberration (-0.92 waves) without correction and the contact lens (plus tear lens) introduces positive spherical aberration of varying amounts. It was found that more highly curved contact lenses on the eye over correct and the flatter contact lenses do not completely correct the negative spherical aberration of the eye. The contact lens base curvatures which maximize the Strehl ratio correspond to those which zero

the spherical aberration as shown in figure 4.11. The model demonstrates that the contact lenses (with the tear lens) can compensate for the higher order spherical aberration of the rat eye in combination with a spectacle lens, therefore improving image quality compared to an aberration corrected spectacle lens alone. In combination with a spectacle lens, the focus on the retinal surface is defined and defocus and spherical aberration are corrected. A contact lens that matches the corneal radius of curvature and simultaneously zeros the defocus and spherical aberration without the use of a supplemental spectacle lens would require aspheric surfaces. For example, a lens with a base curvature that matches the corneal curvature of 2.68mm, with a front curvature of 2.72mm and a conic of -0.081 does not require a spectacle lens and has a Strehl ratio of 0.98.

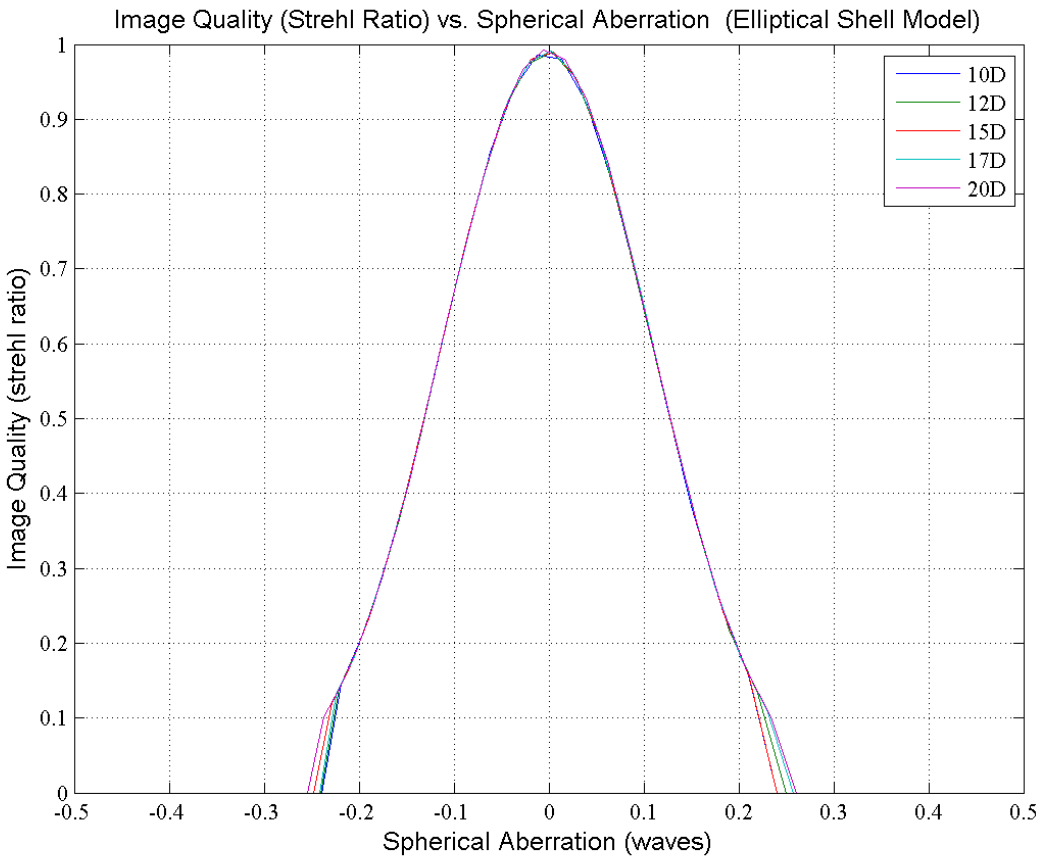

Figure 4.11: The x-axis is RMS spherical aberration (waves), the y-axis is the (unnormalized) Strehl ratio. The image quality reaches a peak when the spherical aberration of the contact lens, tear lens and rat eye combined is zero. Each curve is for a given contact lens nominal power but the base and front surface curves vary to vary the spherical aberration.

4.4.2 Further optical modelling of the rat eye

The refraction of the contact lenses on the second rat did not match up with the predictions of the ESH model with a contact lens and tear lens combination. The model predicts for a contact lens with base curvature of 3.1mm and 12D nominal power required an additional +9D spectacle lens to image the retinal surface however, rat 2 required -1D correction using a 12D contact lens. From Campbell's experimental measurements over a group of

rats ranging from 115 to 140 days, the average center corneal curvature was found to be 2.86mm (Campbell, 1982). The corneal curvature of the second rat may have been closer to the average value across the larger age group. We therefore modified the schematic rat eye model with a new corneal curvature of 2.86mm (Campbell, 1982) to calculate changes in refractive error and spherical aberration relative to retinal surface of this model for the rat eye as a function of the contact lens worn.

The model was modified by changing the radius of curvature of the cornea and axial length of the eye to maintain the refractive error as the previous model for a 2mm pupil. The model had a new corneal curvature of 2.86mm and an axial length to the retinal surface of 6.12mm (original model axial length was 5.99mm). A 12D nominal power contact lens with a base curvature of 3.1mm was used for a 3.5mm pupil on the rat eye to compare the refractive error and spherical aberration as a function of the contact lens worn relative to the retinal surface.

We found with the modified model and 12D contact lens that there was a residual -1.21D of defocus and the spherical aberration was -0.23 waves. In comparison, the second rat with the contact lens had -1D of defocus and -0.42 waves of spherical aberration. There is better agreement between the modified model and the HS measurements of the second rat indicating that the difference between the results and the original model can be explained by a difference in corneal curvature.

4.5 Discussion

4.5.1 Comparing Refractive Error Measurements to the Elliptical Shell Model

We used white light for retinoscopic measurements and a wavelength of 550nm in the ESH model. When comparing the model predictions of refractive error to the retinoscopic measurements, it is assumed that the reflex of light comes from the surface of the retina. Although the retinoscope uses white light, it has been suggested that the reflected light may be shifted towards the red end of the spectrum (Millodot, 1978) giving a 2.5D hyperopic shift from monochromatice green light. Determining the refractive error from the eye model is complicated by the large amount of over-corrected spherical aberration. If we choose to minimize the spot size on the retinal surface, the refractive error, relative to the retinal surface, is 4.8D for a 2mm pupil and 9.4D for a 3.5mm pupil in the ESH model. During retinoscopy, the experimenter neutralized the reflex from the centre of the pupil, so we expect closer agreement with the 2mm refraction than the 3.5 mm refraction. It was determined through experimental measurements by Millodot and Sivak, under the assumption the retinoscopic measurement comes from the retinal surface there would be 8.9D hypermetropia (Michel Millodot, 1978). We measured 12D refractive error with the retinoscope for both rats. The difference between the predicted (4.8+2.5D) and measured retinoscopy values (12D) could arise from difficulty in ignoring the more hyperopic reflex from the edge of the pupil during the measurement, the age difference between the modelled and measured rats or a true variability in refraction due to variation in the optical properties of the eye. Our rats are more hyperopic than some other reports for pigmented rats. (M. Glickstein, 1970, M.C.W. Campbell, 1981)

Comparing the HS measurement to the retinoscope measurement of refractive error in the same rat, we measured 15.8D refractive error with the HS device (830nm light) for the first rat with an aberration corrected spectacle lens in place and 12D refractive error measurement with the retinoscope (white light), a difference of 3.8D. The expected chromatic aberration is 4.6D between 550nm to 830nm, calculated using a water eye model with a 300D eye and the dispersion of water. The spherical aberration of the eye is expected to make the HS refraction across the full pupil 4.6D more hyperopic than the retinoscopy (presumed to weight a smaller pupil). However this full correction is not needed to explain the difference between the retinoscopy and the HS refraction. This again suggests that during the retinoscopy, more peripheral rays were weighted, or that the light reflected during retinoscopy is shifted towards the red end of the spectrum (Michel Millodot, 1978). Moreover, infrared light is expected to penetrate deeper into the retina and reflect from the photoreceptor layer requiring additional spectacle lens power to move the light towards the retinal surface. However, after correction for only chromatic aberration the difference between the HS measurement and retinoscope is very small and does not correspond to an 8.9D shift between the surface of the retina and the photoreceptor layer. This suggests that the HS infrared light may also be emanating from a layer closer to the surface of the retina.

4.5.2 The Effects of Contact Lenses on the Optical Quality of the Rat eye

The refractive error of the contact lenses on the first rat qualitatively matches up with the predictions of the ESH model with a contact lens and tear lens combination. The HS

measured refractive error with +12D contact lens, 6D and -1D residual defocus for the first and second rat respectively. The difference in the HS measurement indicates the contact lens was having a different effect on the aberrations and refraction of the rat eye. The initial model predicts that a contact lens with base curvature of 3.1mm and 12D nominal power requires an additonal +9D spectacle lens to image retinal surface. The first rat shows a similar trend as the initial model. The second rat however, exhibited a different trend and compared more closely to the modified eye model which was explained by the difference of corneal curvature between the two models.

From the experimental results and the optical modelling, we showed that the defocus correction varies with the base curvature of the contact lenses. Some base curvatures of the contact lens may require large spectacle lens correction in order to focus on the retinal surface. The modelling results also indicated that the use of contact lenses can reduce the spherical aberration by an order of magnitude dependent on the contact lens. The reduction comes because the spherical aberration of the contact lenses is in the opposite direction to that of the rat eye. The spherical aberration measured in the two rats with contact lenses were both larger than their respective models possibly due to measurement away from the optical axis and variability of the aberrations of the rat eye which can be caused by a variation in corneal curvature. However, the spherical aberration of both models with contact lenses and the experimental measurements of the two rats with contact lenses (-0.6 and -0.42 waves respectively) are much lower than the spherical aberration of the rat eye model without a contact lens (-0.9 waves). This eye model had amounts of spherical aberration consistent with measurements of refraction at varying pupil sizes in

the rat eye (Campbell, 1982). It is possible for spherical aberration to be converted to third order aberrations if the optical elements are decentered with respect to each other or the pupil is decentered. The third and fourth order higher order RMS with contact lenses for the first rat was measured to be 1.2 waves and for the second rat was 0.7 waves. Total 3rd and 4th order HOA is less than the symmetrical model predicts without a contact lens for the second rat. The overall aberrations of the first rat were reduced with a contact lens in place as predicted by the model.

4.5.3 Utilizing the contact lens for improved image quality and two-photon excitation

To utilize the contact lenses for improved image quality, the base curve of the contact lens needs to be flatter than the corneal radius of curvature as shown in figure 4.9. If a significant amount of defocus is measured while using a contact lens, changing the base curvature may improve focus correction without changing the contact lens's nominal power. However, the power on the eye may change, necessitating a change in the supplemental defocus correction. Therefore, using contact lenses with range of base curvatures is recommended to reduce the spherical aberration of the eye as well as the defocus.

From the image quality versus base curvature (figure 4.9) it appears that adaptive optics may not be required for a two photon excitation experiment. However, in figure 4.9, the Strehl ratio rapidly decreases away from the peaks as the base curvature changes, due to the presence of spherical aberration. The model predicts that contact lenses would work well on-axis, however it is likely images will be away from the optical axis of the eye. The model also assumed axial symmetry however it is known that decentrations of the

optics will introduce higher order aberrations. Campbell's model also demonstrated that the aberrations increased away from the optical axis (Campbell, 1982). Therefore there is potential for image quality improvement from the results shown above, which corresponds to an improvement of probability of two photon excitation, however an adaptive optics set up is still recommended due to the variability of aberrations and corneal curvature and how rapidly the aberrations increase away from the ideal contact lens parameters.

4.6 Conclusions

It was shown that the contact lenses, which were chosen to correct the refractive error of the rat eye, as determined by retinoscopy, did not provide their nominal power by comparing independent HS measurements of the contact lens correction and the spectacle lens correction. Through modifications of the schematic eye model with a contact lens, it was found that the back surface curvature of the contact lens (with nominal power held constant) and the resulting tear lens had a significant effect on the power of the contact lens on the eye, as a result of the mismatch of the back curvature of the contact lens and front corneal curvature and the spherical aberration of the two elements.

For all contact lenses modelled on the eye, the magnitude of spherical aberration decreased. Experimentally HS spot quality improved and the total 3rd and 4th order aberrations reduced. The negative spherical aberration of the rat eye could potentially be completely compensated for using custom fit contact lenses on the rat eye, as shown from the optical modelling of lenses and the improved image quality attained by one animal with a contact and spectacle lens correction. It was determined that a TPE experiment would

benefit from the use of contact lenses for more localized light delivery to the rat retina. Utilization of the contact lens can correct defocus and spherical aberration and therefore less demand would be placed on the adaptive optics mirror for wavefront correction.

Chapter 5

Discussion and Conclusions

5.1 Discussion

We were able to design and construct a diffraction limited AOSLO by integration of a wavefront sensing channel and the Xinetics deformable mirror into the existing Waterloo CSLO. We successfully minimized the system aberrations, specifically astigmatism due to the large telescopes used to magnify the light onto the 47mm Xinetics deformable mirror. We were able to present images of the rat retina, imaging blood vessels suitable for two photon excitation of a photosensitive drug. We obtained video images of the rat retina showing blood flow (which were shown in the thesis defense).

We demonstrated reasonable Hartmann-Shack spot quality with the use of a contact lens and spectacle lens combination. From the model we showed contact lens and spectacle lens combinations can compensate defocus of the eye and tear lens while reducing spherical aberration and higher order aberrations. We also showed that there is great variability of the contact lens corrective power on the rat eye if the contact lens base curve has a significant mismatch relative to the expected corneal curvature which creates a tear lens.

Generally contact lenses are used to correct the refractive error of the eye well enough to potentially allow adaptive optics to correct the residual aberration, however we showed in theory, that with the correct selection, a contact lenses can correct defocus and improve image quality without the use of AO. More importantly, the correction of higher order aberrations would result in less demand on the stroke of the adaptive optics mirror. Bird showed that at large pupil sizes the spherical aberration was significant enough to reduce the probability of TPE and recommended adaptive optics to achieve TPE in a vessel in the rat eye (Bird, 2006). The use of rigid contact lenses could in theory allow for good correction of spherical aberration and full utilization of the f-number of the rat eye before using adaptive optics. To take advantage of the contact lens for the minimization of the spherical aberration having a range of base curves for each nominal power is recommended.

To carry out a TPE experiment, the use of adaptive optics in conjunction with rigid contact lens is still recommended because of optical variations of the rat eye. Although the rigid contact lenses have a beneficial effect in lowering the higher order aberrations, the ESH model assumed axial symmetry. It is known that decentration of the optics will introduce higher order aberrations. The higher order aberrations of the rat eye measured in addition to spherical aberration indicate that the optical elements of the real eye may be decentered rather than axially symmetric. Campbell demonstrated that aberrations increased away from the optical axis (Campbell, 1982) and here we demonstrated that the two slightly different optical models were needed to predict the effect of the contact lens correction on the eyes of two different rats. Adaptive optics would enable the reduction of the aberrations away from the optical axis as well as aberrations due to decentration

of the optics of the eye and the variability between animals. Reduction of the aberrations would in turn increase the probability of TPE.

From the image quality and base curvature figure it appears that adaptive optics may not be required for a two photon excitation experiment. However, In figure 4.11, the Strehl ratio rapidly decreases away from the peaks if the spherical aberration is not completely corrected. The presence of approximately 0.075 waves RMS spherical aberration lowers the Strehl ratio by 20% and the probability of two photon excitation by 40%. In addition, if AO is used, the contact lens chosen would not need to precisely correct the spherical aberration. Spherical aberration correction is sensitive to the base curve chosen (Fig. 4.9) The model predicts that contact lenses would work well on-axis, however it is likely images will be away from the optical axis of the eye. Campbell's model also demonstrated that the aberrations increased away from the optical axis (Campbell, 1982). Therefore there is potential for image quality improvement from the results shown above, which corresponds to an improvement of probability of two photon excitation. However an adaptive optics correction is still recommended due to the variability of aberrations and how rapidly the probability of two photon excitation decreases in the presence of small amounts of aberration.

Another limiting factor we encountered while imaging the rat eye was that our rat holder did not provide precise movements of the rat pupil relative to the exit pupil of the AOSLO. The resulting lack of centration of the rat pupil in the HS arm, or asymmetry within the rat eye's optics, may have contributed to the large amount of higher order aberrations other than spherical aberration, measured by the HS. To improve the rat holder, micrometer

translation stages is recommended to control the x,y, and z axis of the rat. Rotational axes about the body (head to tail axis) of the rat as well as rotation around the z-axis going through (approximately) the pupil of the eye would allow for accurate positioning of the eye relative to the projection of the AO mirror in the eye. The increased precision of the rat holder would allow for reliability between repeated measurements and imaging of the rat eye and reproducibility of the experiment. The use of eye tracking and/or a paralytic in addition to the isoflurane anesthetic may also help reduce eye movement during a TPE experiment. We used spectacle lenses to minimize the defocus and optically slice the rat retina. A Badal optometer could provide a continual adjustment of defocus and optical slicing.

5.2 Conclusions

In conclusion, we demonstrated that we could sense the aberrations of the rat eye with a non-scanning beam. With the results presented we were able to demonstrate that we could image the rat retina with the adaptive optics scanning laser ophthalmoscope. We encountered variable refractive error correction of the rat eye with the contact lenses and extended the Campbell and Hughes schematic rat eye model to model the eye with a contact lens in place with an associated tear lens. Using the model, we determined the contact lens can be used to minimize the spherical aberration of the rat eye model. We demonstrated that the tear film and surface curvatures of the contact lens significantly impact the defocus and spherical aberration of the contact lens on the rat eye. We also optimized the parameters of the contact lens to minimize the large spherical aberration of the rat eye and showed that improved image quality is possible with rigid contact lenses. In turn, this reduces the amount of stroke required by a deformable mirror to correct wavefront aberration. Thus, it should be possible to use a lower stroke adaptive optics mirror such as the Xinetics 37-actuator deformable mirror to correct the aberrations of the rat eye in combination with rigid contact lenses and a spectacle correction.

Chapter 6

Permissions

The following is an email from Dr. Khurana granting permission for the use of figure 1.1 of her thesis.

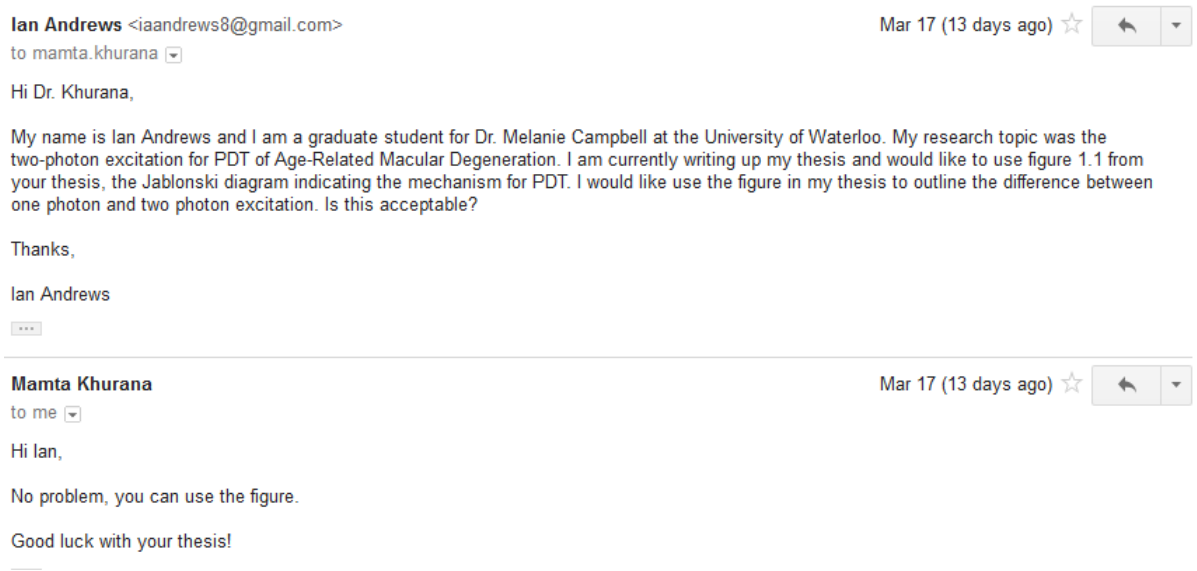

Ian Andrews <iaandrews8@gmail.com> Mar 17 (13 days ago)

to mamta.khurana

Hi Dr. Khurana,

My name is Ian Andrews and I am a graduate student for Dr. Melanie Campbell at the University of Waterloo. My research topic was the two-photon excitation for PDT of Age-Related Macular Degeneration. I am currently writing up my thesis and would like to use figure 1.1 from your thesis, the Jablonski diagram indicating the mechanism for PDT. I would like use the figure in my thesis to outline the difference between one photon and two photon excitation. Is this acceptable?

Thanks,

Ian Andrews

Mamta Khurana Mar 17 (13 days ago)

to me

Hi Ian,

No problem, you can use the figure.

Good luck with your thesis!

References

J.A. Parker A. Chaudhuri, P.E. Hallett. Aspheric curvatures, refractive indices and chromatic aberration for the rat eye. *Vision Res.*, 1982.

M. Bird. Modeling light delivery into the rat eye for two-photon excitation photodynamic therapy treatment of age-related macular degeneration. Master's thesis, University of Waterloo, 2006.

M. C. W. Campbell. *Gradient Refractive Index Opticsand Image Quality in the Rat Eye*. PhD thesis, Australian National University, 1982.

Ronald Cubalchini. Modal wave-front estimation from phase derivative measurements. *J. Opt. Soc. Am.*, 1979.

Yin L Merigan WH Sharma R Libby RT Williams DR Geng Y, Dubra A. Adaptive optics retinal imaging in the living mouse eye. *Biomedical Optical Express*, 2012.

Scott M. MacRae Geunyoung Yoon, Seth Pantanelli. *Optimizing the Shack-Hartmann Wavefront Sensor*. SLACK Inc., 2004.

Tsukasa Nagaoka Darin E. Olson Peter M. Thulé Machelle T. Pardue Govind Nair,

Moon Kim and Timothy Q. Duong. Effects of common anesthetics on eye movement and electroretinogram. *Doc Ophthalmol*, 2011.

Hao F. Zhang Hao Li, Wenzhong Liu. Investigating the influence of chromatic aberration and optical illuminationo bandwidth on fundus imaging in rats. *Journal of Biomedical Optics*, 2015.

Eduardo H. Moriyama Adrian Mariampillai Emma Dahlstedt Milan Balaz Marina K. Kuimova Mikhail Drobizhev Victor X. D. Yang David Phillips Aleksander Rebane Brian C. Wilson Harry L. Anderson Hazel A. Collins, Mamta Khurana. Blood-vessel closure using photosensitizers engineered for two-photon excitation. *Nature Photonics*, 2008.

Eugene Hecht. *Optics 4th ed.*, chapter •. Addison Wesley, 2002.

C. Y. Hooper and R. H. Guymer. New treatments in age-related macular degeneration. *Clinical and Experimental Ophthalmology*, 2003.

Shinji Ohkubo Hisashi Takeda Kazuhisa Sugiyama Ichiro Kawaguchi, Tomomi Higashide. In vivo imaging and quantitative evaluation of the rat retinal nerve fiber layer using scanning laser ophthalmoscopy. *IOVS*, 2006.

David Cramb Ira Probodh. *Two Photon Excitation Photodyanmic Therapy: Working Toward a New Treatment for Wet Age-Related Macular Degeneration*. CC BY, 2012.

Rama D. Jager, William F. Mieler, and Joan W. Miller. Age-related macular degeneration. *New England Journal of Medicine*, 2005.

Peter K. Kaiser. Verteporfin photodynamic therapy combined with intravitreal bevacizumab for neovascular age-related macular degeneration. *American Academy of Ophthalmology*, 2009.

Mamta Khurana. *Two-Photon Excitation Photodynamic Therapy for Localized Blood Vessel Targeting*. PhD thesis, University of Toronto, 2010.

M. Millodot M. Glickstein. Retinoscopy and eye size. *Science, New Series*, 1970.

Anthony Kim Yumi Moriyama George Netchev Margarete K. Akens Harry L. Anderson Mamta Khurana, Sebastien Ulrich and Brian C. Wilson. Biodistribution and pharmacokinetic studies of a porphyrin dimer photosensitizer (oxdime) by fluorescence imaging and spectroscopy in mice bearing xenograft tumors. *Photochemistry and Photobiology*, 2012.

A. Hughes M.C.W. Campbell. An analytic, gradient index schematic lens and eye for the rat which predicts aberrations for finite pupils. *Vision Research*, 1981.

Jacob Sivak Michel Millodot. Hypermetropia of small animals and chromatic aberration. *Vision Research*, 1978.

Donald T. Miller Nathan Dolbe. *Wavefront Correctors for Vision Science*, chapter 4. John Wiley and Sons, Inc., 2006.

Tatiana V. Tkatchenko and Andrei V. Tkatchenko. Ketamine-xylazine anesthesia causes hyperopic refractive shift in mice. *J. Neurosci Methods*, 2010.

C Dai A Camesa H F. Zhang X Liu, C H. Wang and S Jiao. Effect of contact lens on optical coherence tomography imaging of rodent retina. *Curr Eye Res*, 2013.

Phillip Bedggood Xiaolin Zhou and Andrew Metha. Limitations to adaptive optics image quality in rodent eyes. *Biomedical Optics Express*, 2012.

MV. Sarunic Y. Jian, RJ. Zawadzki. Adaptive optics optical coherence tomography for in vivo mouse retinal imaging. *Journal of Biomedical Optics*, 2013.

Robert Wolfe Daniel C. Gray Jennifer J. Hunter Alfredo Dubra John G. Flannery David R. Williams Ying Geng, Kenneth P. Greenberg and Jason Porter. In vivo imaging of microscopic structures in the rat retina. *Invest Ophthalmol Vis Sci.*, 2009.